# Progress towards a $^{39}$K Bose-Einstein Condensate Apparatus

**Sukhman K. Singh**


Physics

August 23, 2023

# Progress towards a $^{39}$K Bose-Einstein Condensate Apparatus

**Sukhman K. Singh**

Dissertation
Master of Science in Physics
University of Toronto
Canada

submitted by
Sukhman K. Singh

Toronto, On August 23, 2023

Supervisor: Prof. Joseph H. Thywissen
First examiner: Prof. Aephraim M. Steinberg
Second examiner: Prof. Dvira Segal
Date of oral exam: August 30, 2023

# Contents

# List of Figures

# Abstract

This thesis presents the progress towards building and designing a new $^{39}$K Bose-Einstein Condensate (BEC) experimental apparatus with tunable interactions. $^{39}$K has several broad magnetic Feshbach resonances that are well characterized by prior work. We plan an all-optical cooling sequence that begins with loading atoms in a 3D MOT from a 2D MOT, followed by gray molasses cooling and evaporation within a crossed optical dipole trap. Currently, we have obtained a 3D MOT and are in the process of implementing $\Lambda$-enhanced gray molasses cooling. Utilizing the Feshbach resonances in $^{39}$K will allow for tuning the interactions between atoms to study quantum dynamics. We plan to turn interactions off in studies of transmission and reflection times of a tunnelling BEC, and conduct atomic Fabry-Pérot experiments.

# Preface

This thesis is based on the an experimental apparatus that was already partially constructed by preceding students. Bernie Hsu has already constructed the vacuum system. Felic Stubenrauch set-up the saturation absorption spectroscopy set-up and electronics utilized for laser locking. Hanzhen Lin built the 2D MOT with permanent magnets. Grace Li and Harish Ramachandran had already constructed the 2D, 3D MOT and gray molasses optics. G. Li and H. Ramachandran had together obtained a 3D MOT. Kelly Smith had written the original time-of-flight (TOF) sequencing, based on the sequencing used in the lattice experiment.

When I joined the team, the MOTs were not operational and optical components in the saturation absorption spectroscopy and the 2D MOT frequency-shifting set-ups were missing. Over the first few months I assisted Nick Mantella on the aforementioned optics. Later on, I revived the 3D MOT optics with Mohammed Mohid. I was involved in replacing the vortex lasers with the new Toptica laser for $D_2$ and $D_1$ cooling and I set-up the laser locking for the $D_2$ line with the new controller and recently impart the $D_1$ laser locking. Mojtaba Khavaninzadeh has been working on $D_1$ optics which are underway of being incorporated into the experiment.

All the data shown in Chapter 3 is taken by M. Mohid and I, including the 3D MOT loading, fluorescence imaging and TOF data. M. Mohid worked on the image processing to generate the TOF thermometry plot, with extensive discussions that involved Cora Fujiwara, Harshil Neeraj and myself. TOF was halted for some time due to the switching circuit not functioning, which H. Neeraj, M. Mohid and I worked on with Robert Morley's help (Electronics Support Services). H. Neeraj operated and tested the Adwin for remote control of the various drivers and updated the sequencing code based on K. Smith's and the lattice experiment. I designed the Optical Dipole Trap optics, based on the ones used for the lattice experiment and calculated the polarizabilities for the dipole trap, illustrated in Chapter 4. All Gross-Pitaevski (GPE) simulations, discussed in Chapter 5, were done by N. Mantella.

Above all, Prof. Joseph Thywissen has directed this project from its infancy and more recently alongside Prof. Aephraim Steinberg to its current state.

# Chapter 1

# Introduction

The principle of Bose-Einstein condensation is not only applicable in the field of ultracold atoms but in a plethora of contexts that involve high energy physics, astophysics as well as condensed matter systems. Bose condensation of multi-hadron matter has also been observed in the hexaquark d*(2380) [1]. This particle existed [1] for $10^{-23}$ sec [25] and it is hypothesized that BECs composed of such hexaquarks in the early universe could portray dark-matter like behaviour [3]. Quasiparticles in solids, such as magnons [14] carry an integer spin of 1 and thereby is described by Bose-Einstein statistics. Bose condensed magnons were observed at 14 K in an antiferromagnetic material, and later it was even observed at room temperature in a ferromagnetic material [33, 12]. The density of atoms in condensed matter system is much greater than that in dilute gas experiments which attributes to the larger transition temperatures. Magnons also have smaller masses, that is on the order of the electron mass, as opposed to neutral atoms. External magnetic fields are used to control the magnon densities, or equivalently the magnon chemical potential. This allows access to a variety of magnon densities ranging from strongly interacting Bose liquid up to a dilute Bose gas.

## 1.1 Motivation

What do you need for a Bose-Einstein Condensate?

Merely three things, in priciple:

- Bosons: We use $^{39}$K . The critical aspects of the choice of the atom are discussed in Section 1.2.

- Above critical phase-space density: The experiment is being designed so that it would employ an all-optical cooling scheme.

- Reason: The scientific goals are discussed extensively in Chapter 5).

[1] Lifetime obtained from energy-time uncertainty principle, where $\Gamma \approx 70$ MeV for $d^*(2380)$.

## 1.2 Why $^{39}$K?

The tunability of interaction via the scattering length is highly desirable. This is because Feshbach resonances in this species allow for zero-interactions. The experimental goals of this apparatus entail gaining access to the zero-crossings near the $^{39}$K Feshbach resonances which are further elucidated in Chapter 5.

A close competition for the new generation experiment was $^{85}$Rb since it is used for another experiment in the department. However an all optical path does not work for $^{85}$Rb due to issues with the scattering cross section which make it practically difficult to condense and it only has one Feshbach resonance. Another candidate was $^{87}$Rb. Its largest width Feshbach resonance occurs at 1007 G with a width $\Delta = 170$ mG and the next one is at 600 G with $\Delta = 17$ mG [30]. A high fractional stability $\delta B/B_0$ in the magnetic field generated with the Feshabach coils is required. The field stability required is quatified by the fluctuations $\delta B$ and it is dictated by two factors: the width of the Feshbach resonance $\Delta$ and the *in situ* measurement of the magnetic field.

The first condition $\delta B \ll |\Delta|$ must apply where the resonance width $\Delta$ ranges from 10 mG to 100 G [52]. Broader magnetic Feshbach resonance widths at lower magnetic fields are therefore highly desirable. While narrow resonances, found in alkaline earth metals and non-zero angular momentum channels (e.g. $d$-wave resonances), are practically harder to attain [56].

Secondly, *in situ* measurement of the field constrains the field stability. Often, the field inside a vacuum chamber is characterized via transitions between two-magnetic manifold in the trapped atoms, such as with Rabi spectroscopy. The Rabi frequency $\Omega$ of a transition is bound by the particular transition and the micro-wave (mw) or radio-frequency (rf) power accessible. Thus, at the Feshbach resonance $B_0$, $\delta f = \frac{df}{dB}|_{B_0}\delta B \lesssim \Omega/(2\pi)$ where $\delta f$ are the fluctuations in the transition frequency.

$^{39}$K has numerous Feshbach resonances [13] at relatively low magnetic field. These would require less fractional stability in the magnetic field, in comparison to other alkali species.

## 1.3 General Properties

Potassium was discovered in 1807 by the chemist Sir Humphry Davy who developed it from caustic potash (potassium hydroxide, KOH). Potassium was the first of the metals to be isolated from electrolysis in pure active form with a melting point of T = 336.8 K. Prior to the alkali and alkaline earth metals, including sodium and calcium, were known in their compound form. Although conducting the electrolysis experiment allowed him to obtain metallic, it would rapidly react with water or air to default into its compound form. Metallic potassium is often submerged in mineral oil for storage, in order to prevent it from reacting with the water vapour and oxygen in atmosphere [53, 27].

Potassium finds many applications in commercial technology. It forms compounds, most common of which is with chlorine (KCl) that is used in fertilizers and as salt. In

certain types of nuclear reactors, an alloy with sodium (NaK) is utilized as a liquid coolant due to its high thermal conductivity which allows for effective heat transfer. In the medical field, particularly in respiratory equipment it is utilized to produce $O_2$. By burning metallic potassium in air, the oxidizer potassium superoxide ($KO_2$) forms on the metal surface. Potassium superoxide undergoes the reaction $2KO_2 + H_2O + 2CO_2 \rightarrow 2KHCO_3 + O_2$ to generate diatomic oxygen $O_2$.

Potassium possesses seventeen known isotopes, two of which are stable and both have bosonic statistic, $^{39}$K and $^{41}$K. The fermionic radioactive isotope $^{40}$K has a half-life of $1.3 \times 10^9$ years with two decay channels. These three isotopes comprise ordinary potassium. The $^{39}$K isotope is high abundant, 93.25 %, and hence impart why it is a desirable candidate [11].

## 1.4 Electronic Properties

Potassium is appealing for quantum gas experiment due to its energy structure that results from its electronic strucure. Its electronic ground state it has the configuration of $[\mathrm{Ar}]\, 4s^1$. It has a full p-shell configuration similar to the nearest noble gas of Argon and a single valence electron in an incomplete 4s-orbital. This level structure provides the possibility of laser cooling.

The bosonic isotopes of potassium $^{39}$K and $^{41}$K have a a nuclear spin quantum number of $I = 3/2$. The total electronic angular momentum $\mathbf{J}$ leads to the fine structure and it originates from the coupling of the orbital angular momentum $\mathbf{L}$ of the valence electron and the spin angular momentum $\mathbf{S}$. The $LS$-coupling is given by $\mathbf{J} = \mathbf{L} + \mathbf{S}$ has values of J ranging from $|\mathrm{L} - \mathrm{S}| \leq \mathrm{J} \leq \mathrm{L} + \mathrm{S}$. For the first excited state ($L = 1$), the spin-orbit coupling lifts the degeneracy of $2^2P_{1/2}$ and $2^2P_{3/2}$ yielding to the splitting in $D_1$ and $D_2$ spectral lines. The corresponding $J = 1/2$ and $J = 3/2$, respectively. For light elements LS coupling is often observed as the Coulomb interaction stronger than the spin-orbit interaction. Whereas for heavy ones higher order interaction occur; the spin-orbit interaction dominates over or is on the order of the Coulomb interaction which gives rise to the $jj$-coupling where remaining electrons couple independently.

The hyperfine interaction arises from the coupling of the nuclear spin $\mathbf{I}$ with the total electronic spin $\mathbf{J}$, such that $\mathbf{F} = \mathbf{I} + \mathbf{J}$. The two excited state can be distinguished since fine structure splitting for excited state is $\Delta E = h \times 1.73$ THz with respect to the smaller perturbation of the hyperfine interaction. The hyperfine structure of the $2^2P_{1/2}$ excited state has $F' = \{1, 2\}$ level that differ by 55.5 MHz. The $2^2P_{3/2}$ state has $F' \in [0, 3]$ where the stretched state are only split by 33.8 MHz so it does not have a well-resolved hyperfine structure.

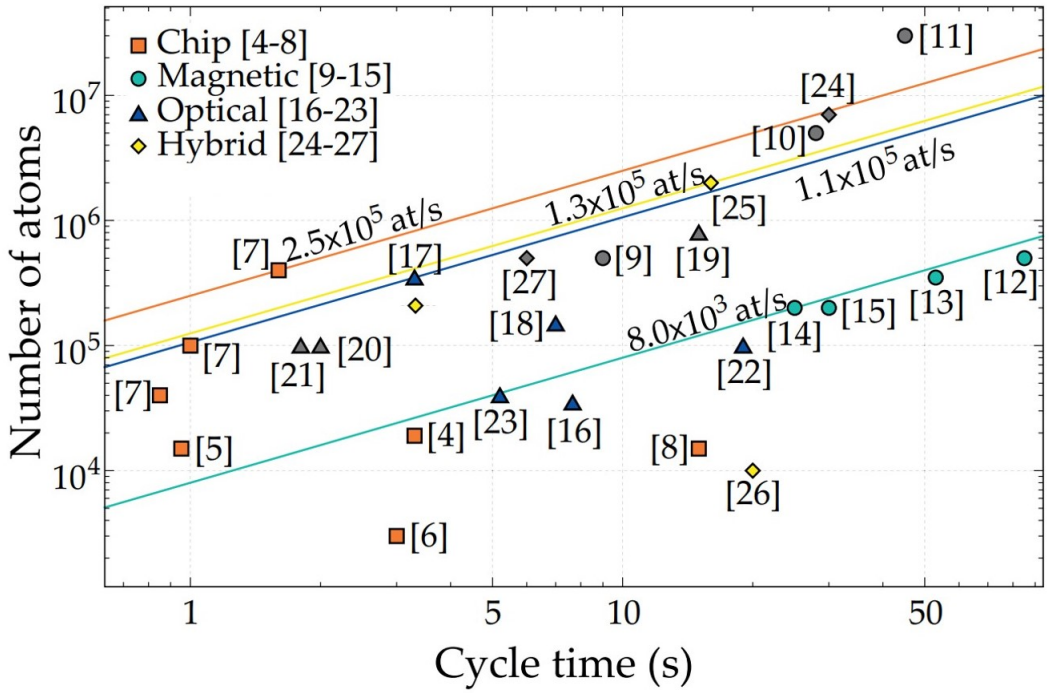


Figure 1.1: Comparison of various BEC experiments based on the cycle times: chip-based experiments (orange), magnetic traps (teal), all-optical cooling (blue) and hybrid consisting of a magnetic-trap and optical cooling. Adapted from [37]

## 1.5 Magnetic Properties

Potassium has a relatively small nuclear magnetic momentum compared to other alkalis. The nuclear spin of $^{39}$K is 3/2 and a magnetic moment of 0.39.

## 1.6 Scattering Properties

Thermalization of the atoms is determined by the scattering parameters and thus it is the key property in evaporative cooling process. Scattering can be ellucidated by the radial Schrodinger equation. At ultracold temperature, the relative angular momentum $L$ of the scattering particles is $L = \hbar\sqrt{l(l+1)} \approx \hbar r/\lambda_{th} \ll \hbar$ for the relevant temperatures. Here, $r$ is the interaction range that is typically 10-100 $a_0$, Bohr radii and $\lambda_{th}$ is the thermal de Broglie wavelength. Thus, at the admissible densities and temperatures $l \ll 1$ and since $l$ is an integer, it must hold that $l = 0$. The scattering then diminshed to $s$-wave scattering for ultracold atoms and only the lower partial waves are significant. A potassium dimer can either be a single ($S = 0$) or a triplet ($S = 1$) since its spin is $s = 1/2$. The untuned, background $s$-wave scattering length of $^{39}$K is 138.49 $a_0$ for the singlet and -33.49 $a_0$ for the triplet [18]. For quantitative description, the scattering length can be compared to the

van der Waals potential.

## 1.7 Outline

The proposed experiment aims to be an all-optical evaporation cooling scheme of $^{39}$K. The choice of an all-optical path is justified as follows [20]. Fig.1.1 depicts the production of various BEC experiments. The majority of experimental work has been carried out with rubidium (coloured) or sodium atoms, both of which have positive scattering lengths that amount to repulsive interactions, discussed further in Section 2.3. Atom chip based experiments (orange) which are outperforming in terms of the most atom numbers attained for the smallest relative cycle. Although atom chip based cooling would promise short preparation times, it can lead to detrimental light scattering on the chip surface. Additionally, chip experiments do not provide sufficient optical access. An all-optical path to degeneracy would not rely on an external magnetic field and thus it would not necessitate particular magnetic properties. Evidently, magnetically trapped clouds are comparatively worst by an order of magnitude in atom numbers as the fraction of atoms in a magnetically non-trappable states is disposed.

Chapter 2 introduces the theory behind Bose-Einstein condensates.

Chapter 3 presents the theory of the cooling and trapping techniques used alongside to the state of the current set-up.

Chapter 4 describes the new additions to the Bose-Einstein condensation apparatus and the design considerations.

Chapter 5 investigates future directions and the scientific goals that the experiment aims to tackle.

# Chapter 2

# Bose-Einstein Condensates

A primordial property of Bose-Einstein condensates is that a large fraction of the particles are found in the same lowest-energy state. This can be verified by measuring the velocity distribution of the atoms. Here, we summarize the basic theory behind Bose-Einstein Condensates at zero temperatures. All of the information summarized in this chapter can be found in greater detail and elegant analysis in sections of [35] and [51].

## 2.1 Boson Statistics

When the inter-particle spacing $d$ is comparable to their thermal de Broglie wavelength

$$d \approx \lambda_{th} \tag{2.1}$$

with

$$\lambda_{th} = \sqrt{\frac{2\pi\hbar^2}{mk_BT}} \tag{2.2}$$

the wavefunction of individual particles begins to overlap. Below the critical temperature $T_c$ the group of atoms is described by a single wavefunction.

### 2.1.1 Critical Temperature

The temperature below which a fraction of a thermal ensemble starts to form a Bose-Einstein condensate is known as the critical temperature $T_c$. This temperature is a function of the density of atoms $n$, how strongly they interacting - that is quantified by the scattering length $a$, and the mass $m$ of atoms involved. By dimensional analysis, the critical temperature is deduced to be

$$T_c \propto \frac{\hbar^2}{k_Bm} n^{3/2} \tag{2.3}$$

or equivalently a critical number density $n_c$

The fraction of the cloud that condenses is the fraction of atoms in the ground state $N_{gs}$. Thus, the condensate fraction $N_{gs}$ goes as

$$\frac{N_{gs}}{N} = \frac{N - N_{excited}}{N} = 1 - \left(\frac{T}{T_c}\right)^{3/2} \tag{2.4}$$

for $T < T_c$. A finite critical temperature only exists in 3D [23]. For instance, an ideal gas confined in a 3D harmonic potential.

## 2.2 Bose-Einstein Condensate Theory

### 2.2.1 Gross-Pitaevski Equation

The Gross-Pitaevski equation describes a non-uniform Bose gas at zero-temperature when the scattering length of the particles is much less than the inter-particle spacing. The interaction between particles is treated in the Hartree or mean-field approximation. The state of a BEC can be described in terms of the condensate wavefunction $\Psi(\mathbf{r})$ [9, 35].

The energy associated with $\Psi(\mathbf{r})$ in the mean field approximation the many-body wavefuction $\Psi(\mathbf{r})$ is the symmetrized product of all single-particle states. The symmetrization for identical bosons, requires that all the coefficients in the many-body wavefunction are equal. If they were not equal, then upon particle exchanges the total wavefunction could be changed. Thus, any term in the wavefunction can be turned into any other with particle exchange. For a fully condensed state, all bosons are found in the same single-particle state $\psi(\mathbf{r})$. The $N-$particle wavefuctions is then [35]

$$\Psi(\mathbf{r}_1, \mathbf{r}_2, ..., \mathbf{r}_N) = \prod_{i=1}^{N} \psi(\mathbf{r}_i) \tag{2.5}$$

for normalized single-particle wavefunction $\int d\mathbf{r}|\psi(\mathbf{r})|^2 = 1$. The wavefunction of the condensate state can be written as $\Psi(\mathbf{r}) = N^{1/2}\psi(\mathbf{r})$. The density of particles for this system is given by $|\Psi(\mathbf{r})|^2$ such that the total number of particles is

$$N = \int d\mathbf{r}|\Psi(\mathbf{r})|^2 \tag{2.6}$$

the energy of the system is $\langle\Psi(\mathbf{r})|\,\hat{H}\,|\Psi(\mathbf{r})\rangle$. In the mean field approach, the interactions $g$ are accounted for explicitly. The energy then is

$$E(\Psi) = \int d\mathbf{r}\left(\frac{\hbar^2}{2m}|\nabla\Psi(\mathbf{r})|^2 + V(\mathbf{r})|\Psi(\mathbf{r})|^2 + \frac{1}{2}g|\Psi(\mathbf{r})|^4\right) \tag{2.7}$$

where the inter-particles interaction, that is the coupling constant $g$, is proportional to the scattering length $a$ of two interacting bosons is

$$g = \frac{4\pi\hbar^2 a}{m} \tag{2.8}$$

The effective interaction $g$ is for describing interactions between very long wavelength excitations and at low energies. The contact interaction of two particles at positions $\mathbf{r}$ and $\mathbf{r}'$ is $g\delta(\mathbf{r}-\mathbf{r}')$.

We can obtain an expression for $\Psi(\mathbf{r})$ though the method of Lagrange multipliers. That is, by minimizing the energy in 2.7 with respect to infinitesimal variations in $\Psi(\mathbf{r})$ and with the condition that the number of particles given by 2.6 is kept constant. With Lagrange multiplier for contant particle number $\mu$ which interpreted as as the chemical potential, the Lagrangian function becomes $\delta E - \delta\mu = 0$. The variations are taken to be with $\Psi$ and $\Psi^*$ independently. The gradient with respect to $\Psi^*$ yields the time-independent Gross-Pitaevski equation for some external potential $V$ (e.g. a harmonic trap)

$$-\frac{\hbar}{2m}\nabla^2\Psi(\mathbf{r}) + V(\mathbf{r})\Psi(\mathbf{r}) + g|\Psi(\mathbf{r})|^2\Psi(\mathbf{r}) = \mu\Psi(\mathbf{r}) \tag{2.9}$$

where the chemical potential $\mu$, from thermodynamics, is the energy associated with the addition or removal of a particle in the system. The Gross-Pitaevski equation has the form of the Schrödinger equation with an additional non-linear term in the wavefunction $\Psi(\mathbf{r})$. The potential exerted in the particles is the sum of the external potential $V$ and the due to the quadratic term $g|\Psi(\mathbf{r})|^2$ which arises from the mean field approximation. The non-linear term $g|\Psi(\mathbf{r})|^2$ is proportional to the density of atoms $|\Psi(\mathbf{r})|^2$ times the effective interaction $g$. Thus, the interaction energy at position $\mathbf{r}$ accounts for the mean field produced by other bosons at that position.

The dynamics of a BEC are governed by the time-depedent Gross-Pitaevski equation

$$i\hbar\frac{\partial\Psi(\mathbf{r})}{\partial t} = \left(-\frac{\hbar}{2m}\nabla^2 + V(\mathbf{r}) + g|\Psi(\mathbf{r})|^2\right)\Psi(\mathbf{r}) \tag{2.10}$$

#### 2.2.1.1 Limitations of GP

The Gross-Pitaevski model is based on the assumption that the interactions between atoms are due to two-body contact [35]. This condition is valid for dilute gases of Bose-Einstein condensates in three-dimensions. To compensate for condition, higher-order power of the wavefunctions must be added to the Schrödinger equation. Indeed, one must go beyond the Gross-Pitaevski equation to determine the scaling of the speed of sound in Helium-4 [44]. to the logarithmic Schrödinger equation with the term $\psi ln|\psi|^2$ added to the GP equation, along with a sextic contribution $|\psi|^6$ that accounts for three-particle interactions [44, 5].

### 2.2.2 Thomas-Fermi Approximation

Although the Gross-Pitaevski equation is already a simplification of a real BEC, as it is derived under mean-field approximation, it is a non-linear Schrödinger equation nonetheless. It does not have a generic exact solution. So, we can implement reasonable approximation in the presence of a trapping potential $V$.

For sufficiently large clouds the kinetic energy becomes negligible. Predominantly for strong enough interactions since if there are no interactions the cloud size does not matter,

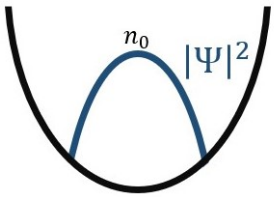


Figure 2.1: Probability distribution $|\Psi|^2$ of ground state occupation $n_0$ under the Thomas-Fermi approximation.

i.e. atom number $\times$ scattering length becomes important. When the number of atoms is large and interaction are repulsive. If the kinetic energy of the atoms is much less than the potential energy then we can neglect the kinetic energy term and eq. 2.9 simplifies to

$$V(\mathbf{r})\Psi(\mathbf{r}) + g|\Psi(\mathbf{r})|^2\Psi(\mathbf{r}) = \mu\Psi(\mathbf{r}) \tag{2.11}$$

This simplification is known as the *Thomas-Fermi approximation*. Solving the Gross-Pitaevski equation in the Thomas-Fermi limit gives the ground state energy as

$$n(\mathbf{r}) = |\Psi(\mathbf{r})|^2 = \frac{\mu - V(\mathbf{r})}{g} \tag{2.12}$$

for $\mathbf{r}$ where $\frac{\mu - V(\mathbf{r})}{g} > 0$ and 0 elsewhere. We can obtain a scaling for the atomic density $n$ at the centre of the cloud $n_0$ for a harmonic potential $V(\mathbf{r}) = \frac{m\omega_0^2}{2}r^2$, using the normalization condition $\int d\mathbf{r} n(\mathbf{r}) = 1$ as $n_0 \sim N^{2/5}$.

## 2.3 Interactions for Low Energy Atoms

Without interactions, it would not be possible to cool atoms down since they would not be able to re-distribute their energy and momenta. Neutral atoms comprising a dilute gas interact via van der Waals interactions ($\sim 1/r^6$ at large distances), predominantly. At ultra-cold temperatures, interactions dominate since the atomic gas tends to condense into the lowest energy single-particle state and the kinetic energy is suppressed. Thus, nearly all aspects of cold atoms involve interaction effects between atoms [6]. Thus, we make two important assumptions:

- The temperature of the gases is extremely low

- The gases are very dilute

The implications of these observations are as follows. At ultralow temperature the two-body interatomic interaction potential simplifies to an effective potential $U_{\text{eff}}$. In the low energy limit, the effective interaction between two atoms at position $\mathbf{r}$ and $\mathbf{r}'$ is

$$U_{\text{eff}}(\mathbf{r}, \mathbf{r}') = U_0\delta(\mathbf{r} - \mathbf{r}') = \frac{4\pi a\hbar^2}{m}\delta(\mathbf{r} - \mathbf{r}') = T^{2B}\delta(\mathbf{r} - \mathbf{r}') \tag{2.13}$$

where $T^{2B}$ is the two-body scattering matrix [51], $a$ is the $s$-wave scattering length accounting for all the two-body interactions and $m$ is the atomic mass.Two particles scatter via $s$-waves. This can be understood in terms of the relative angular momentum of the scattering partners. At temperature $T$, the relative angular momentum $\mathbf{L}$ will be on the order of $O(\hbar/\lambda_{th})$ where $\lambda_{th}$ is the thermal de Broglie wavelength. That is, in terms of the interaction range $\mathbf{r}$, the relative angular momentum is $\mathbf{L} \approx \mathbf{r} \times \mathbf{p}$. Typically, the interaction range $r$ is 10-100$a_0$, Bohr radii. At low temperatures ($kr_0 \ll 1$), we note $|L| = \hbar\sqrt{l(l+1)} \approx \hbar r/\lambda_{th} \ll \hbar$, that is the integer $l \ll 1$. Hence, $l = 0$ and the particles undergo $s$-wave scattering. Secondly, cold atomic gases are typically dilute gases which implies that two-body scattering events are more likely than multi-body collisions since particle separation is on the order $O(100nm)$. Thereby, heating of the gases due to scattering particles is quenched. Such two-body scattering can be either elastic or inelastic. Elastic collisions are responsible for thermalization in the cloud while inelastic lead to collisional losses that reduce the lifetime of the cloud.

### 2.3.1 Scattering matrix

The standard approach for understanding scattering is through the method of *partial waves*. For rotationally invariant potential, the wavefunctions $\psi(r, \theta, \phi)$ are conviniently labelled with their angular momentum $l$. Wavefunctions that are independent of $\phi$, $\psi(r, \theta) = \sum_{l=0} R_l(r) P_l(\cos\theta)$. These can be expanded in terms of partial waves with the Legendre polynomials $P_l(\cos\theta)$ as an eigenbasis that solves the Schrondinger equation for the *relative* motion of the colliding particles. The total scattering cross-section is proportional to sum the of all phase shifts due to scattering with all the possible angular momenta $l$.

#### 2.3.1.1 Phase Shift

An incident plane wave with wavevector $\mathbf{k}$ scattering-off of a particles, interacts with a scattering potential. Via the scattering process it picks up a phase $\phi$. An infinitesimal cross-sectional area $d\sigma$ would scatter-off at an infinitesimal solid angle $d\Omega$ such that the total scattering cross-section is given by

$$\sigma = \int d\Omega \frac{d\sigma}{d\Omega} \tag{2.14}$$

The outgoing wave, is a spherical wave that is modulated by a scattering amplitude $f(\mathbf{k}, \frac{\mathbf{r}}{r})$. For a dilute gas, parametrizing the eigenenergies with the Schrödinger equation $H\psi_{\mathbf{k}} = E_{\mathbf{k}}\psi_{\mathbf{k}}$ results in the scattering states $\psi_{\mathbf{k}}(\mathbf{r})$

$$\psi_{\mathbf{k}}(\mathbf{r}) = e^{i\mathbf{k}\cdot\mathbf{r}} + f\left(\mathbf{k}, \frac{\mathbf{r}}{r}\right) \frac{e^{i\mathbf{k}\cdot\mathbf{r}}}{r} \tag{2.15}$$

where $e^{i\mathbf{k}\cdot\mathbf{r}}$ is the incoming plane wave and $\frac{e^{i\mathbf{k}\cdot\mathbf{r}}}{r}$ is the outgoing scattering wave. As the magnitude of the scattered wave vector, $k \to 0$, the phase shift $l = 0$ dominates. For cold

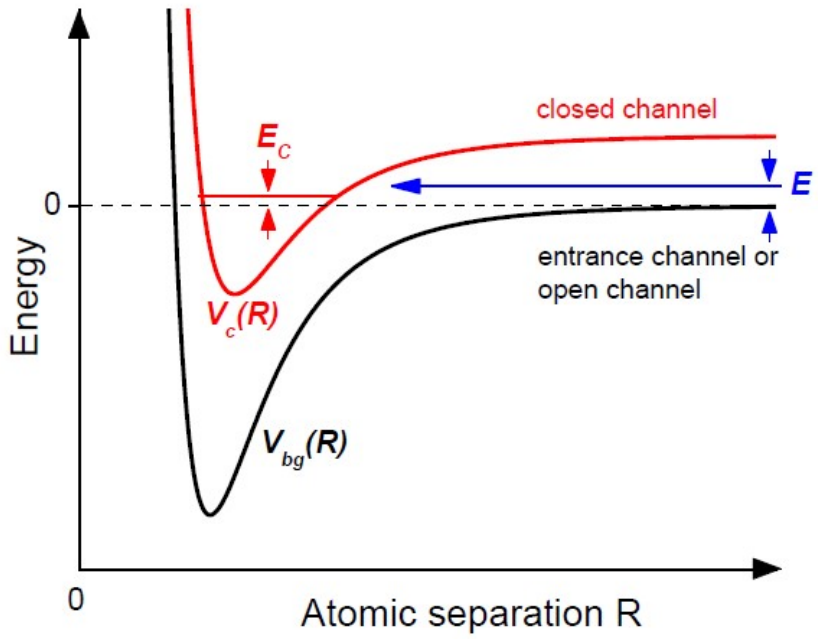


Figure 2.2: Principle for Feshbach resonance. Two scattering atoms coming at collision energy $E$, where $V_{bg}(R)$ is their collision potential as a function of their separation (R) see an inter-atomic potential. Feshbach resonance occurs when the collisional energy $E_c$ of atoms is coupled with the closed channel ($V_c(R)$) with energy $E$. Taken from [6].

gases, below 100 nK, the contribution from higher partial waves that have higher angular momenta become negligible during collisions.

There is a subtle change in the scattering theory for identical particles. The collisional cross-section in standard scattering theory is $4\pi a^2$. However, for identical bosons there is an additional factor of 2 in the scattering cross-section. The energy-depedent s-wave cross-section $\sigma$ at low energies for identical bosons

$$\sigma = 8\pi a(k)^2 \tag{2.16}$$

Positive scattering length $a(k)$ amount to repulsive interactions while negative scattering length correspond to attractive ones. Low temperature alkalis with two-body interactions have a repulsive potential at small distances due to the significant overlap of the electron cloud. Whereas, at larger distances the interactions become attractive (van der Waals) and scale as $1/r^6$.

### 2.3.2 Feshbach Resonances

Resonances are of particular interest in scattering theory. Magnetic Feshbach resonances are appreciable in ultracold atomic physics due to their tunability of the scattering length.

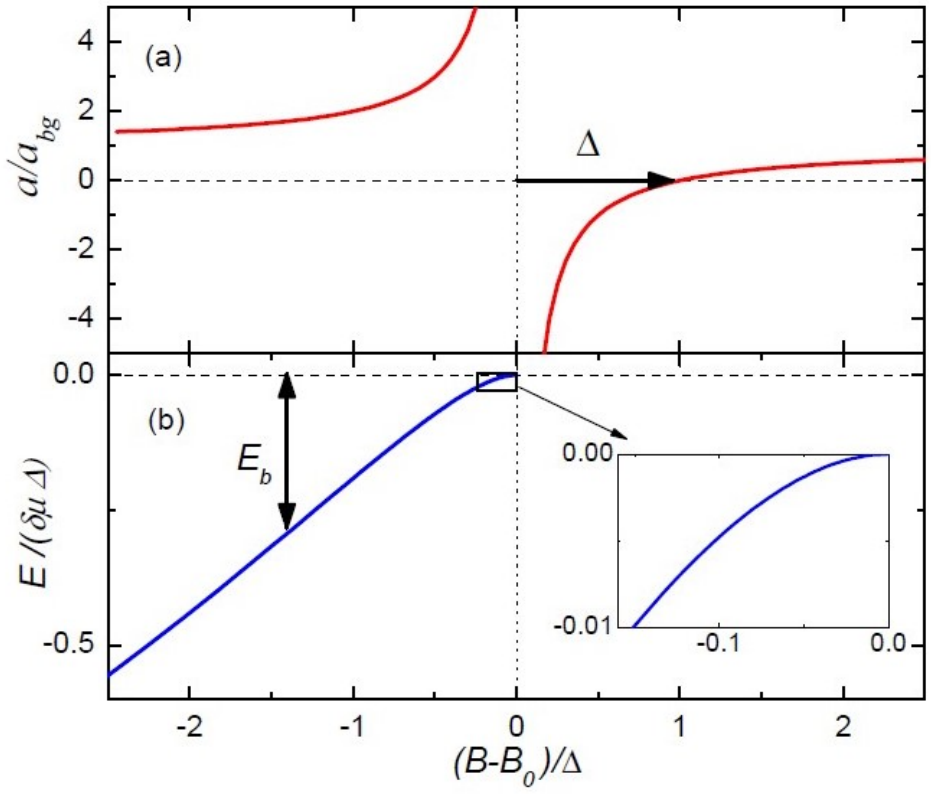


Figure 2.3: Scattering length $a(B)$ of two scattering atoms near Feshbach resonance (top). The equation for scattering length $a(B)$ is given in 2.18 with width $\Delta$ and untuned scattering length of $a_{bg}$. The binding energy $E_b$ is given by equation 2.20 for Feshbach molecules which form at positive scattering lengths $a(B)$ (bottom). Taken from[6]

In many-body systems composed of ultracold atoms, a scattering process can result in weakly bound molecules for certain magnetic fields, known as Feshbach molecules. These molecules form when the kinetic energy of two colliding atoms ($E_c$) is the same as the bound state energy ($E_b$) of the interatomic potential. Feshbach resonances occur when the bound state of the closed channel is tuned to resonance with the collision energy of the scattering particles. The open channel is energetically accessible for a collision process with some small energy $E$. The closed channel can accommodate a molecular bound state when it energetically approaches the scattering state in the open channel. When the corresponding magnetic moments are different, resonant coupling can be achieved by an external magnetic field that is used to magnetically tune to a Feshbach resonance.

These channels correspond to different spin configurations of the atomic pair in ultracold collisions. Thereby, the internal state energies can be modulated via external magnetic fields. The two channels are coupled by the hyperfine interaction and the resonances occur when the bound state is tuned near threshold $\tan\eta$ where $\eta(E)$ is the scattering phase

| $\|F, m_F\rangle$ | $B_{\text{res}}$ (G) | $a_{\text{bg}}\Delta$ ($a_0$ G) | $B_{\text{zero}}$ (G) | $\bar{\mu}(\mu_B)$ |
|---|---|---|---|---|
| $\|1,1\rangle$ | 25.91(6) | - | - | −0.605 |
| $\|1,1\rangle$ | 402.74(1) | 1530(20) | 350.4(1) | −0.961 |
| $\|1,1\rangle$ | 752.3(1) | - | - | −0.987 |
| $\|1,0\rangle$ | 58.97(12) | - | - | −0.337 |
| $\|1,0\rangle$ | 65.57(23) | - | - | −0.370 |
| $\|1,0\rangle$ | 472.33(1) | 2040(20) | 393.2(2) | −0.945 |
| $\|1,0\rangle$ | 491.17(7) | 140(30) | 490.1(2) | −0.949 |
| $\|1,-1\rangle$ | 33.5820(14) | −1073 | / | 0.324 |
| $\|1,-1\rangle$ | 162.36(2) | 760(20) | / | −0.489 |
| $\|1,-1\rangle$ | 561.14(2) | 1660(20) | 504.9(2) | −0.959 |

Figure 2.4: Feshbach resonances in $^{39}$K. The resonaces occur at $B_{res}$ with effective width $a_{bg}\Delta$ and corresponding zero crossing at $B_{zero}$. The atomic-state magnetic moments are given by $\mu_B$ at the resonance $B_{res}$. Taken from [17]

shift, near $k \to 0$.

If particles interacting under the influence of a potential $V(\mathbf{R})$ that varies as $1/R^s$, such as a Van der Waals potential where $s = 6$, the threshold $\tan\eta$ goes as $k$ and $k^3$ for $s$- and $p$-wave scattering. For $s$-wave collisions, the effective range expansion of $\tan\eta_0$ with $k$ gives

$$\cot\eta_0(E) = -\frac{1}{ka} + \frac{1}{2}r_0 k \tag{2.17}$$

where $a$ is the $s$-wave scattering length with values $(-\infty, \infty)$ based on the potential, $r_0$ is the effective range and $\hbar k$ is the relative momentum of the colliding atom-pair. That is, for low energies ($k \to 0$) the interaction between two particles can be quatified by a single quantity - the scattering length $a$. Near Feshbach resonance, the range of interaction between a scattering pair is parametrized by the $s$-wave scattering length $a(B)$:

$$a(B) = a_{bg} - a_{bg}\frac{\Delta}{B - B_0} \tag{2.18}$$

where $a_{bg}$ is the background scattering length, $\Delta$ is the width of the Feshbach resonance and $B_0$ is the magnetic field at which the resonance occurs.

Due to the bosonic nature of $^{39}$K, the two-atom scattering state is symmetric

$$|12\rangle = \frac{1}{\sqrt{2}}(|1\rangle_1 |2\rangle_2 + |2\rangle_1 |1\rangle_2). \tag{2.19}$$

Above a resonance, such a quasi-bound dimer has energy

$$E_b = \frac{\hbar^2}{2m_r a^2} \tag{2.20}$$

where $m_r$ is the reduced mass of the two colliding $^3$9K atoms and $a$ is the scattering length as identified in 2.18.

# Chapter 3

# Laser Cooling and Trapping: Experimental Set-up

Laser cooling and trapping was developed by S. Chu, C. Cohen-Tannoudji and W. D. Phillips [22, 7, 10]. Laser cooling is extensively used in a plethora of fields. Gravitational fields are measured with ultra high precision from the doppler shift of free falling atoms on Bloch oscillations. Optical clocks that are based on the ultracold atoms. And, of course, the most interesting of them all, creating Bose-Einstein Condensate with ultracold gases. Here we discuss the theory behind laser cooling and trapping of neutral atoms and the current state of the experimental apparatus.

## 3.1 Doppler-free Saturation Absorption Spectroscopy

In theory, atomic lines are $\delta$ functions. In reality, the absorption lines broaden via the following mechanisms:

### 3.1.1 Doppler Broadening

An atom at rest sees an incident photon with angular frequency $\omega$ with the same frequency. However, radiation that has an angular frequency $\omega$ in the laboratory reference frame is Doppler shifted in the frame of a moving atom by

$$\omega^{'} = \omega - \mathbf{k} \cdot \mathbf{v} \tag{3.1}$$

where $\mathbf{k}$ is the wavevector of the incident light field. The component of velocity $v$ that is in the direction of the wavevector $k$ leads to the first order Doppler shift, hence it is $\mathbf{k} \cdot \mathbf{v}$.

For a non-interacting gas of atoms at some tempererature $T$, the atomic velocities are distributed according to the Maxwell-Boltzmann distribution $f(v)$. For an infinitesimal speeds of atoms in the range $v$ to $v + dv$, the fraction of atoms with this velocity class is

$$f(v)d^3v = \sqrt{\frac{m}{2\pi k_B T}} e^{-\frac{mv^2}{2k_B T}} d^3v \tag{3.2}$$

where $m$ is the mass of the identical atoms in the gas. At temperature $T$, the most probable speed of atom is $v_p = \sqrt{\frac{2k_BT}{m}}$ obtained by setting $\frac{df(v)}{dv} = 0$ while the mean velocity is $\bar{v} = 2\frac{v_p}{\sqrt{\pi}}$, obtained from the first-order moment of $f(v)$.

We can obtain the shape of an absorption spectrum for an atom cloud with respect to the angular frequencies of a incident radiation field. By noting that in the rest frame of an atom, it will absorb an incident photon at the resonance frequency $\omega_0$ while an atom moving at velocity $v$ will absorb it when $\delta = \omega - \omega_0 = kv$ which gives

$$\frac{v}{c} = \frac{\delta}{\omega_0} \tag{3.3}$$

this is a relation between the frequency of the radiation and the atomic velocities. Thus, the absorption feature using 3.2 is

$$f_D(\omega) = \frac{c}{v_p\omega_0\sqrt{\pi}} e^{-\left(\frac{c}{v_p}\frac{\delta}{\omega_0}\right)^2} \tag{3.4}$$

where the detuning $\delta = \omega - \omega_0$. The absorption $f_D(\omega)$ has a Gaussian shape and results in the inhomogenous broadening of the spectral lines due to the motion of atoms. This is known as the *Doppler broadening* of the spectral lines.

### 3.1.2 Sub-doppler Broadening

Thus far, we have ignored the finite linewidth $\Gamma$ of an atomic transition. Due to the natural linewidth, caused by the finite lifetime of an excited state, the atom can absorb a range of frequencies associated with the width of the transition. This results in homogeneous broadening of the absorption lines. Typically, the excited states are short lived state, thus by energy-time uncertainty principle

$$\Delta E \Delta t \geq \frac{\hbar}{2} \tag{3.5}$$

that is, the short lived states have large uncertainties in energy. Thus, the photons emitted from an excited state have a range of frequencies $\Delta\omega \sim \frac{\Delta E}{h} \sim \frac{1}{2\pi\Delta t}$.

Considering a cloud of atoms in excited state, the amplitude $E(t)$ describing the number of atoms found in the excited state is $E(t) = E_0 e^{-\Gamma t}$. A monochromatic wave has a single frequency component $a(\omega)e^{i\omega t}$.The amplitude $E(t)$ can be obtained as the superposition of monochromatic waves $\int_{-\text{inf}}^{\text{inf}} d\omega a(\omega)e^{i\omega t}$. Taking Fourier transform and then evaluating the resultant integral gives the coefficients $a(\omega)$. The spectral distribution of the intensity $I(\omega) = |a(\omega)|^2$ which has the form of a Lorentzian (3.6) modulated by a factor of $E_0^2$.

While the inhomogeneous Doppler broadening is described by a Gaussian as seen in 3.1.1, the homogeneous broadening is described by a Lorentzian function

$$g(\omega - kv) = \frac{\Gamma/(2\pi)}{(\delta - kv)^2 + \Gamma^2/4} \tag{3.6}$$

where $\Gamma$ is also interpreted as the damping rate of the oscillator in the Lorentz oscillator model of optical response of atoms.

### 3.1.3 Frequency-modulated (FM) Saturated Absorption Spectroscopy

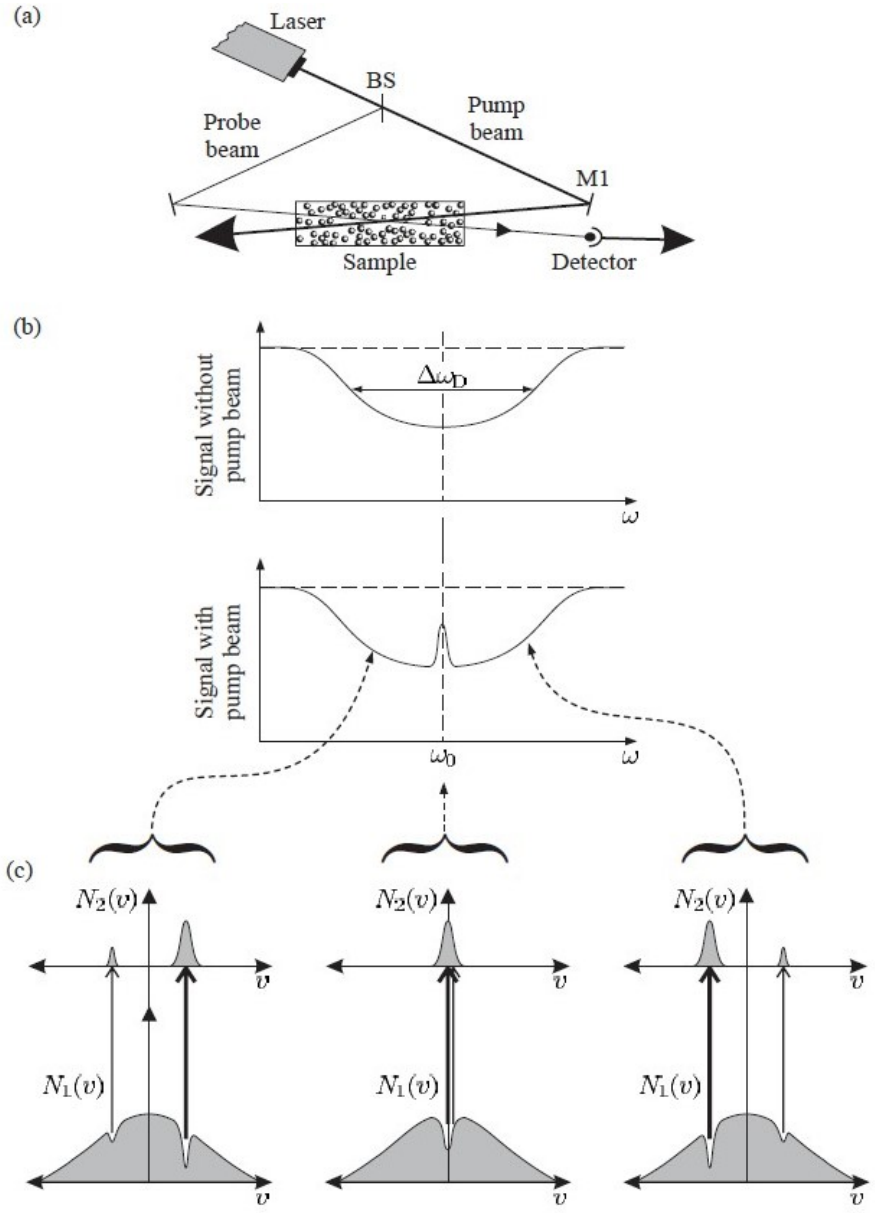


Figure 3.1: Saturation absorption spectroscopy (SAS). (a) Set-up for SAS involving counter-propagating pump and probe beams. (b) Doppler broadened photodiode signal (top) and signal with sub-doppler features (bottom). (c) Longitudinal velocity in the direction of the probe beam propagation for a two-level system. The beam frequency increases towards right. Taken from ref.[19].

At room temperature, Doppler broadening predominates over the homogeneous broad-

ening mechanisms, including the natural width of the transition. To avoid the issue of Doppler broadening without cooling the atoms down to the millikelvin scale, a pump-probe spectroscopic technique is used. At room temperature doppler broadening is the dominant broadening mechanism. $v/c$ room temperature atoms is $10^{-6}$ from equation 3.3, $\delta$ = few * $10^{-6}$ *$10^{14}$ Hz = few* 100 MHz.

In saturated absorption spectroscopy the saturation of absorption is used to generate a Doppler-free signal. At high laser intensities, greater than the saturation intensity $I_s$ associated with a transition, the populations distribution in different energy sublevels becomes uniform such that the population difference between the ground and excited state vanishes for a two-level system under saturation. However, the uniform distritbuion of multiple sublevel for real systems does not necessarily occur, under the condition of saturation absorption, unless the beam is unpolarized. The presence of multiple sublevels results in a *cross-over signal* in the absorption spectrum.

In the pump-probe scheme, a low intensity probe beam ($I_{probe} \ll I_s$) propagates through a vapour cell and the intensity is measured on a photodiode. A high intensity pump beam ($I_{pump} \gtrsim I_s$) counter-propagates the probe beam. Without the pump beam, the absorption signal would only entail the Doppler broadened feature. The pump and probe beams have the same frequencies but they address different atoms depending on their velocity class, that is, due to the thermal motion.

On resonance ($\delta = 0$) and under saturation due to the strong pump beam, the ground and excited states are equally populated. The pump beam interacts with atoms with velocity $v = (\omega - \omega_0)/k$. If a photon from the probe beam encouters an atom in the excited state, it will undergo stimulated emission. The probe photon will penetrate through the cloud and result in dip in the absorption.

For blue-detuned beams ($\delta > 0$), the pump would address the atom with the velocity class moving away from the pump beam source while the probe would address the ones moving in the opposite direction; and vice versa for red-detuned ($\delta < 0$) beams.

### 3.1.4 Locking on the $^{39}$K $D_2$ and $D_1$ lines

We use frequency-modulated (FM) saturation absorption spectroscopy for the frequency stability of our diode lasers. The probe signal is modulated by an Electro-Optics Modulator and then photodiode signal is de-modulated at $\omega_0$ by a an RF-mixer ([1]). Such modulation and de-modulate is independent of first-order fluctuations in temperature and pressure. More details in Ref. [50].

#### 3.1.4.1 Electro-Optical Modulators (EOMs)

The probe beam is phase-modulated using an Electro-Optical Moddulator (EOM [2]). An EOM is used to create frequency-sidebands in the same spatial mode as the monochromatic probe beam $Ae^{i\omega t}$. The phase shift $\phi$ is proportional to the electric field applied inside the

[1] Mini-Circuits ZFM-3-S+ mixer for the $D_2$ locking

[2] QUBIG PM7-NIR10*in*$D_2$ locking, Thorlabs EO-PM-NR-C1 in $D_1$ locking

EOM birefringent crystal (often lithium niobate). A sinusoidally varried voltage potential with frequency $\Omega$ is applied to the EOM such that the output mode has a time-dependent phase.

$$Ae^{i\omega t+i\beta sin(\Omega t)} \approx Ae^{i\omega t}\left(1+i\beta sin(\Omega t)\right) \tag{3.7}$$

where the Taylor approximation is taken since the sinusoidal modulation amplitude $\beta$ is small. Upon simplification of the sine, the carrier with the two sidebands in the frequency, $\omega \pm \Omega$ appear in the EOM output

$$A\left(e^{i\omega t}+\frac{\beta}{2}e^{i(\omega+\Omega)t}-\frac{\beta}{2}e^{i(\omega-\Omega)t}\right) \tag{3.8}$$

using the first term in the Taylor expansion. However, there are additional sidebands due to the expansion that are expressed in terms of the Bessel functions but their amplitudes are negligible for the purpose of observing a saturation absorption spectroscopic signal.

The probe beam is frequency modulated at the transition frequency $\omega_0$. The attenuation in a band depends on the frequency of the band. Thus, the sidebands have a different amplitude than the central frequency. This amplitude modulation is linear in the difference in the amplitudes of the two first-order side bands, as shown in Fig.3.2.

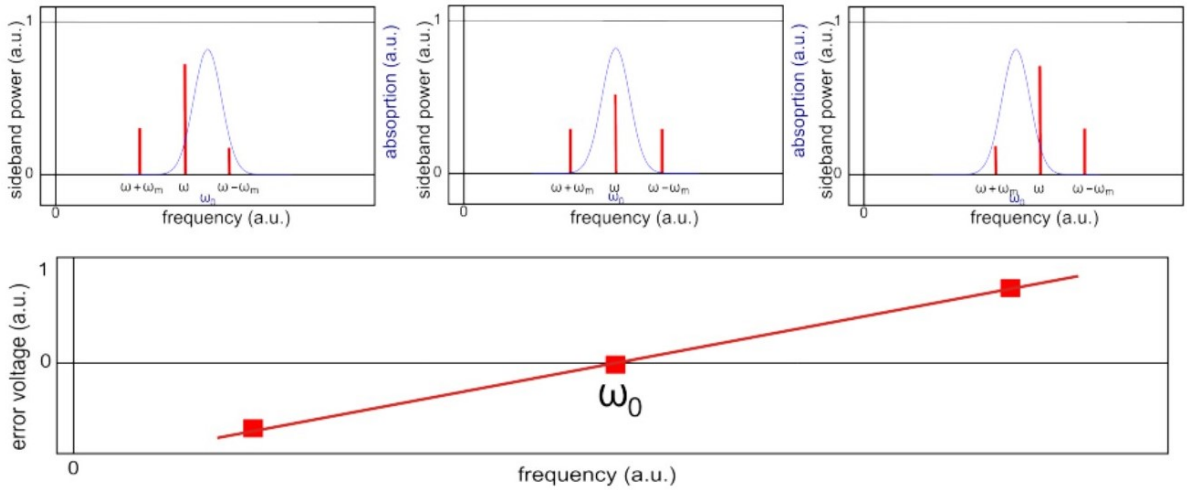


Figure 3.2: Frequency modulated saturation absorption spectroscopy (FM-SAS). An Electro-Optical Modulator (EOM) is used to frequency modulated at the transition frequency $\omega_0$ using modulation frequency $\omega_m$. The sidebands in the beam are attenuated based on the frequency, as shown in the top plots. The difference in the amplitude of in the two sidebands due to attenuation corresponds to a linear attenuation difference, as illustated by the DC error signal in the bottom plot. Taken from [50].

## 3.2 Optics with Matter-Waves: Light Forces & Doppler Cooling

Mechanical forces of light on atoms.

Each time an atom absorbs or emits a photon, its velocity changes due to momentum conservation by the recoil velocity $v_{rec}$

$$v_{rec} = \frac{\hbar k}{m} \tag{3.9}$$

where $k = \frac{2\pi}{\lambda}$ is the wavevector of the light and $m$ is the atomic mass. The scattering rate of photons is close to $\Gamma$ natural linewidth for near resonant light. $\Gamma$ is the inverse of the lifetime of the excited state $\tau$ as implied in the Optical Bloch equations (OBEs) which describes the internal state dynamics (population and coherences). For the $D_2$ line in $^{39}K$, the lifetime is 26 ns. The deceleration due to a resonant photon then is $\Gamma v_{rec} \approx 10^5 \mathrm{m/s}^2$, neglecting the Doppler effect.

For laser cooled atoms, the external time scales are set by the recoil energy $E_{rec} = \frac{m v_{rec}^2}{2}$. In the semi-classical approach, the external motion of the atom is treated classically so as long as two conditions pertaining the position $r$ and momentum $p$ are satisfied. First, the position of the atom is well-defined in comparison to the wavelength of the laser field, that is

$$\Delta r \ll \lambda \leftrightarrow \Delta r \ll k^{-1} \tag{3.10}$$

Secondly, in order for the frequency of the field to be visible to the atom, the atomic velocity is better known than $\frac{\Gamma}{k}$ such that

$$\Delta v \ll \Gamma/k \rightarrow \Delta p \ll m\frac{\Gamma}{k} \tag{3.11}$$

From the uncertainty principle $\Delta r \Delta p \geqslant \frac{\hbar}{2}$, we recover the minimum energy scale, the recoil shift $\frac{\hbar^2 k^2}{2m}$ which is independent of the initial momentum,

$$\hbar\Gamma \gg \frac{\hbar^2 k^2}{2m} \tag{3.12}$$

In the other limit, where $\hbar\Gamma < E_{rec}$ condition, the laser cooling mechanism leads to sub-recoil Doppler cooling. Such a mechanism is used in the cooling scheme of our apparatus, known as Gray Mollases and it is further discussed in Sec.3.5 .

## 3.3 Light Forces

We can obtain the force exerted by a laser field on an atom within the Heisenberg picture [16]. The total atom-light Hamiltonian is

$$\hat{H} = \hat{H}_{atom} + \hat{H}_{Rad} + \hat{V}_{AL} + \hat{V}_{AR} \tag{3.13}$$

with

$\hat{H}_{atom} = \hbar\omega_0 |e\rangle\langle e| \otimes I_{COM} + I_{electronic} \otimes \frac{\hat{\mathbf{p}}^2}{2m}$ where term $|e\rangle\langle e|$ is from the internal electronic degrees of freedom; while the term $\frac{\hat{\mathbf{p}}^2}{2m}$ is for the center of mass (COM) motion

$\hat{H}_{Rad} = \sum_{\mathbf{k},\epsilon} \hbar\omega_{\mathbf{k},\epsilon}\hat{a}^\dagger_{\mathbf{k},\epsilon}\hat{a}_{\mathbf{k},\epsilon}$ for modes of the field defined by the wavevector $k$ and the polarization vectors $\epsilon$

$\hat{V}_{AR} = -\hat{\mathbf{D}} \cdot \hat{E}(\hat{\mathbf{r}}, t)$ is the coupling to the classical field due to dipolar interaction. In the strong coupling regime, the Rabi frequency $\Omega$ gives $\hbar\Omega = -(\mathbf{d} \cdot \epsilon)\mathcal{E}$ with $\mathbf{d} = \langle e|\hat{\mathbf{D}}|g\rangle$ and the electric field is decomposed into the the polarization vector $\epsilon$ as $E = \epsilon\mathcal{E}$

$\hat{V}_{AL}$ is the coupling of the laser field with the quantum field that is responsible for spontaneous emission. This term is ignored in the semi-classical treatment.

The force operator in the Heisenberg representation is

$$\hat{\mathbf{F}} = \frac{d\hat{\mathbf{p}}}{dt} = \frac{1}{i\hbar}[\hat{\mathbf{r}}, \hat{H}] \tag{3.14}$$

where the only non-commuting terms with $\hat{\mathbf{p}}$ come from $\hat{V}_{AR}$ and $\hat{V}_{AL}$. Then the mean force is $\hat{\mathbf{F}} = \langle\hat{\mathbf{F}}\rangle = -\langle\nabla\hat{V}_{AL}\rangle$. The $\langle\nabla\hat{V}_{AL}\rangle$ terms in terms of the dipole operator becomes $\langle\nabla\hat{V}_{AL}\rangle = \langle\nabla(\hat{\mathbf{D}} \cdot \hat{E})\rangle = \langle\hat{D}\rangle\nabla E$ . We note that the average term $\langle\nabla\hat{V}_{AR}\rangle$ vanishes since the momentum kicks due to spontaneous emission are in random $\mathbf{k}$ directions so that they average out to zero. However, Brownian motion in momentum space induced by fluctuations from the random force $\nabla\hat{V}_{AR}$ which is thus non-zero and sets a limit to the final finite temperature achieved in the cooling process.

The total force

$$\mathbf{F}(\mathbf{r}) = -\frac{s}{1+s}\left(\hbar\delta\frac{\nabla\Omega}{\Omega} + \hbar\frac{\Gamma}{2}\nabla\phi\right) \tag{3.15}$$

where $\phi$ is the phase of the electric field and $s$ is the saturation parameter

$$s(\mathbf{r}) = \frac{\Omega^2/2}{\delta^2 + \frac{\Gamma^2}{4}} = \frac{I/I_s}{1 + \frac{4\delta^2}{\Gamma^2}} \tag{3.16}$$

with saturation intensity $I_s$. For $D_2$ transition in $^{39}$K, $I_s$ is 1.75 mW/cm$^2$.

The mean steady-state dipole $\langle\hat{D}\rangle_{ss}$ is obtained from the Optical Bloch equations and has two components. First, a term proportional to $\delta/\Omega$ for some detuning $\delta$ which generates a *conservative force*. This corresponds to the real part of polarizability, it is zero on resonance. It oscillates in-phase with the electric field, proportional to $\nabla\Omega(\mathbf{r})$. Second, a term proportional to $\frac{\Gamma}{2\Omega}$ which results in a *dissipative force*. This is related to the imaginary part of polarizability and it is maximal on resonance. This is in quadrature with the electric field, proportional to $\nabla\phi$.

### 3.3.1 Radiation Force

Photon scattering from an atom causes a mechanical light force applied to the atom by the radiation, know as *radiation pressure force* , is [8, 36]

$$\mathbf{F}_{scatt} = -\hbar(\nabla\phi)\Gamma\rho_{ee} \tag{3.17}$$

where $\rho_{ee}$ is the population of the excited state such that the spontaneous scattering rate is $\Gamma_{sp} = \Gamma\rho_{ee} = \frac{\Gamma}{2}\frac{s}{1+s}$. For a plane wave $e^{i\mathbf{k}\cdot\mathbf{r}}$, the gradient of phase $\nabla\phi = -\mathbf{k}$. The radiation pressure force is in the direction of the *polarization vector* $\boldsymbol{\epsilon}$ rather than the propagation direction of the field. At large velocities, the cooling force scales as $v^{-2}$.

Thus, the mean force is $\mathbf{F}_{scatt} = \Gamma_{sp}\hbar\mathbf{k} = \Gamma_{sp}\hbar k\boldsymbol{\epsilon}$ which occurs due to momentum transfer of in units of recoil $\hbar k$ for each absorption of a photon by the atom. This scattering transfer occurs at a rate of $\Gamma_{sp}$. Since the emission of photons is isotropic, equally probable in all wavevector directions, the atom is 'pressured' to move in the direction of the incident wavevector by the radiation.

#### 3.3.1.1 Dependence on Intensity

On resonance, the saturation parameter $s = I/I_s$, where $I_s = \frac{2\pi\hbar c\Gamma}{3\lambda^3}$ is the saturation intensity. The saturation intensity is a property of each transition and it quantifies the intensity at which the scattering rate is maximal, that is $\frac{\Gamma}{2}$. In the limit of large intensities $I \gg I_s$ which are typically used in experiments, the scattering force also saturates and becomes $\hbar k\frac{\Gamma}{2}$.

#### 3.3.1.2 Dependence on Detuning

The radiation pressure is directly proportional to the scattering rate which is itself dependent on the detuning $\delta$ of the light field. The scattering rate follows a Lorentian shape with width of $\frac{\Gamma}{2}\sqrt{1+I/I_s} = \sqrt{\frac{\Omega^2}{2} + \frac{\Gamma^2}{4}}$ . There is line broadening due to saturation.

Any shifts in the line, either due to the Doppler effect $\mathbf{k}\cdot\mathbf{v}$ or due to the Zeeman effect $g\mu_B B/\hbar$ changes the effective detuning to $\delta' - \delta - \mathbf{k}\cdot\mathbf{v} - g\mu_B B/\hbar$. For large detunings $\delta \gg \Gamma$, the scattering force − and the rate − scales as $1/\delta^2$.

### 3.3.2 Dipole Force

The first term in the total force in 3.15 is responsible for the *conservative force* by a light field on atoms [21, 32]. Explicitly, the *dipole force* is

$$F_{dip} = -\hbar\delta\frac{s}{1+s}\frac{\nabla\Omega}{\Omega} = \frac{-\hbar\delta/2}{1+I/I_s+(2\delta/\Gamma)^2}\frac{\nabla I(\mathbf{r})}{I_s} \tag{3.18}$$

This is a conservative force since it has a corresponding potential

$$U_{dip} = \frac{\hbar\delta}{2}\ln\left[\frac{1+I(\mathbf{r})/I_s}{1+(2\delta/\Gamma)^2}\right] = \frac{\hbar\delta}{2}\ln\left[1+s(\mathbf{r})\right] \tag{3.19}$$

#### 3.3.2.1 Dependence on Intensity

For far off-resonance $|\delta| \gg \Gamma, \Omega$, the saturation parameter $s$ given by 3.16 is very small $s \ll 1$. Thus, Taylor expansion of the logarithm in the dipole potential gives

$$U_{dip} \approx \frac{\hbar\delta}{2} s(\mathbf{r}) = \frac{\hbar\Gamma^2}{8\delta} \frac{I(\mathbf{r})}{I_s} = \frac{\hbar\Omega(\mathbf{r})^2}{4\delta} \tag{3.20}$$

that is, the dipole potential is proportional to intensity for $|\delta| \gg \Gamma, \Omega$.

#### 3.3.2.2 Dependence on Detuning

At zero detuning, on resonance ($\delta = 0$) dipole force vanishes.

Since the dipole force is associated with the real part of the atomic polarizability, it has a dispersive form. That is, the force and the potential have opposite sign for red vs blue detunings. For blue detunings $\delta > 0$, the potential has a positive sign, so at high intensity a blue-detuned beam acts as a repelsive potential. While, for red-detunings $\delta < 0$, the dipole force is attractive (positive).

For far-detuned laser field ($|\delta| \gg \Gamma$), the dipole force goes as $1/\delta$, whereas the radiation force goes as $1/\delta^2$. Thus, the far off-resonant beam can be used to trap atoms within a conservative potential with the right detuning sign.

## 3.4 Magneto-Optical Trap

In this section, we discuss the theory behind the most used cooling technique used in cold-atom experiments, a Magneto-Optical Trap (MOT). Coolings of atoms entails decreasing the temperature, decreasing the entropy or increasing the phase space density. That is, cooling is a process that inherently require dissipation, something that takes away the entropy. Unlike the $D_1$ cooling mechanism in $^{39}K$which does not encompass a trapping force, a MOT is responsible for both cooling and trapping of the atoms.

The dissipative force in action is the *radiation force*, discussed in Section 3.3.1. It is because of the imbalance of the scattering forces from the laser beam moving in the direction of the atom and opposite to it which provides the confinement. The imbalance in the radiation pressure originates from the preferential absorption of particular polarized photons (either $\sigma^+$ or $\sigma^-$). The changing Doppler shift is compensated by a spatially varying magnetic field that bring the atoms back to resonance with the MOT beams. A quadroupole magnetic field (for a 3D confinement) generates a spatially-varying Zeeman shift experienced by the atomic cloud. The magnetic field gradient provides the trapping force while cooling is attained by the scattering force exerted by $\sigma^+$ or $\sigma^-$ photons. The Zeeman shift at displacement $z$ provided by the magnetic field is

$$U_Z = \frac{g\mu_B}{\hbar} \frac{dB}{dz} z \tag{3.21}$$

where $\mu_B$ is the Bohr magneton, $g$ is the Landé $g$-factor, which for many transitions used in laser cooling is $g \approx 1$. While the cooling force originating from the circularly-polarized radiation is proportional to the velocity of the atoms $F_{cool} \propto -\alpha v$.

For a simple two-level atom, an atom moving in the $\hat{x}$ direction will absorb counter-propagating photon and receive a momentum pick of $-\hbar k$, that is in the original direction of the photon. It will spontaneous re-emit the photon after the lifetime of the excited state. During re-emission, the atom will again receive a momentum kick in some random direction. In momentum space, the atom undergoes a random walk. This process is repeated a multitude of times, where photons are spontaneous re-emitted isotropically resulting in net momentum change in the atom such that it undergoes optical molasses.

The force exerted by the MOT beams changes the atomic momentum only until stimulated emission becomes important which occurs for high enough beam intensities. The momentum kick due to stimulated emission is opposite to the recoil momentum kick from the photon absorption which imposes a limit on the maximum deceleration of the atom, $\mathbf{a}_{max} = \hbar \mathbf{k} \Gamma/(2m)$, where $\Gamma/2$ is the inverse of the lifetime of the transition at saturation intensity $I_{sat}$ given in 3.3.1.1; for $^{39}$K, $\mathbf{a}_{max} \approx 40$ km/s$^2$ without considering the doppler effect. The atoms initially coming out of the dispensers are at a temperature of 50 $^oC$ approximately and by equipartition theorem they travel at around 300 m/s. Following the MOT stage, they are cooled down to a few cm/s. Currently, our estimate of the MOT temperature is 4.4 mK.

#### 3.4.0.1 Can any atomic transition be used for a MOT?

No.

At room temperature, atoms are roughly travelling at 440 m/s (from Equipartition theorem), close to the cruising speed of a commercial aircraft. A thermal atom possesses momentum that is thousands of orders of magnitude larger than that of a photon ($p = h/\lambda$). Thus, cooling involves a multitude of absorption-emission cycles, in each of which the atom looses a unit of angular $\hbar k$. As such, the atom must have a particular atomic structure that allows the atom to return to its original atomic state after each cooling cycle. That is, a closed optical loop is required, known as a *cycling transitions*.

Alternatively, if the atom does not have an optical cycling transition, it can still be laser cooled by having a *re-pump* beam. As the name suggests, if the atoms lands in a state that does not comprise the cooling transition, the re-pump beam optically pumped back to the cooling loop. There is no cyclic transition in $^{39}$K, which necessitates the use of two beams, addressing the trap and re-pump transitions which are approximately similar in power. As such, both the trap and re-pump provide cooling forces.

**Transition in $^{39}$K MOT:**

Among the alkalis, potassium is unique in that it has a relatively small nuclear magnetic momentum which results in small hyperfine splitting of the optical transitions. The hyperfine structure of the $D_2$ transition, $P_{3/2}$ excited state is only 33.8 MHz in total compared to the natural linewidth of the transition $\Gamma = 2\pi 6.2$ MHz. $^{39}$K has largest hyperfine interaction splitting for the $P_{3/2}$ state between $F' = 2$ and $F' = 3$ levels which is only

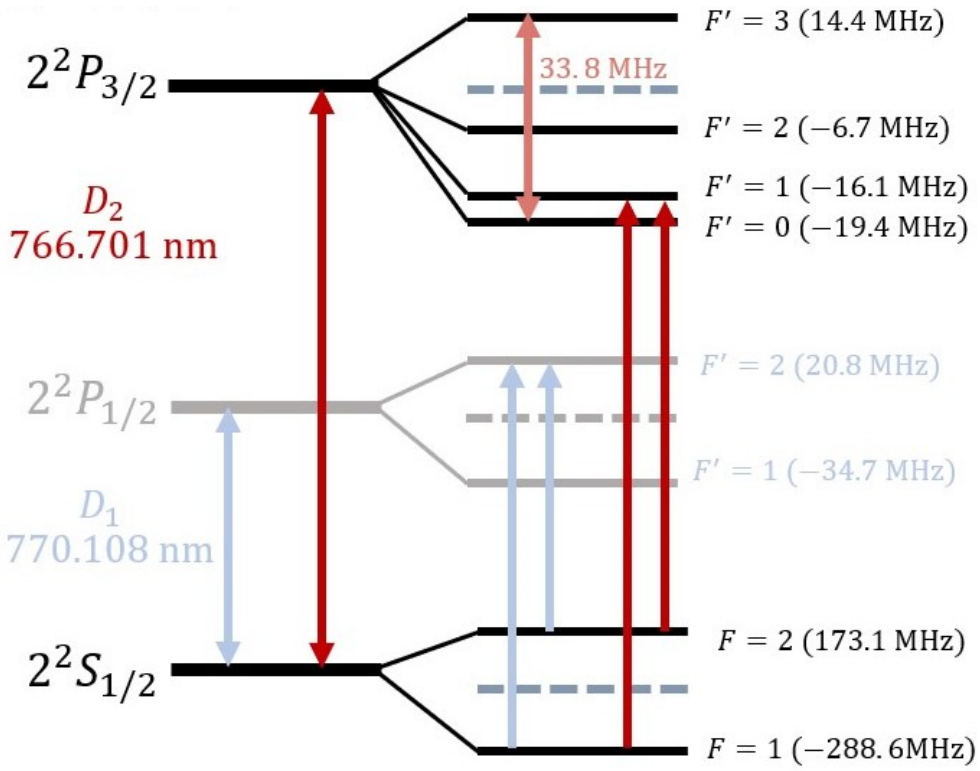


Figure 3.3: Level structure of $^{39}$K. The $D_2$ transition at 767 nm is used for the 2D and 3D MOTs. The $P_{3/2}$ excited state structure is not resolved. $F = 1$ and $F = 2$ ground state manifolds are used for the trap and re-pump beams, respectively. Adapted from [53].

21 MHz. Due to the narrow hyperfine splitting, it would be difficult to address a single transition in the excited state, as the case to other alkalis. The typical transition used in alkalis is $F = 2 \rightarrow F' = 3$. If a red-detuned beam were used to address this transition, the laser will be blue-detuned to the $F' = 0, 1, 2$ transitions. The narrow atomic narrow would lead to a significant portion of the atoms being coupled to the other transitions, that would lead acceleration and heating of the atoms. Thus, the trapping and re-pumping transitions are ideally red-detuned to the entire excited state structure.

#### 3.4.0.2 Capture Velocity of a MOT
#### How slow must an atom move to be caught in a MOT

Capture velocity of MOT: The 2D MOT captures atoms from background vapour pressure, that is from high-temperature vapour generated by the dispensers. The velocities for such a thermal cloud distributed according to the Maxwell-Boltzmann distribution. Only atoms that are below the capture velocity of the MOT are effectively slowed down and trapped by the MOT.

We can estimate the capture velocity by considering the momentum $\mathbf{p}_{beam}$exerted by a

MOT beam of size $L$ and the momentum $\mathbf{p}_{atom}$ of an atom, such that $\mathbf{p}_{beam} = \mathbf{p}_{atom}$. The time it would take an atom travelling at velocity $v$ to traverse the MOT region of length $L$, is simply $L/v$. The maximum radiation force is $F_{max} - \hbar k\Gamma/2$ and thus the capture velocity is $v_c = \frac{\hbar k\Gamma}{2m}$. For $^{39}$K, $v_c \approx 10$ m/s. However, since the excited state hyperfine splitting is not resolved in $^{39}$K (and the trap and re-pump beams are red-detuned in relation to all the excited state transitions), the effective capture velocity is exceeds 30 m/s for the trap.

#### 3.4.0.3 Limits of a MOT

The minimum temperature achievable with MOT is limited by the Doppler temperature. Each cooling cycle consists of two momentum kicks $\hbar k$ - one of these contributes to cooling while the other to heating. The first momentum kick in the direction of initial propagation of a photon and the second from its spontaneous re-emission. The emission of a photon from an atom is isotropic, according to the dipole emission pattern. As such, the surrounding atoms re-absorb the emitted photon which leads to heating.

The lower limit attainble in a MOT is imposed by the momentum recoil kicks from the photon recoil. In momentum space, the atom receives momentum kicks with step size of $k$. The fluctuations in the random walk in the velocity of the atom, that is the mean-square atomic momentum $< p^2 > \neq 0$. In the steady state where the heating and cooling rates equilibrate, the limit is by the Doppler cooling limit $T_D$

$$T_D = \frac{\hbar\Gamma}{2k_B} \tag{3.22}$$

where $\Gamma$ is the transition linewidth and $k_B$ is the Boltzmann constant. For $^{39}$K, the doppler temperature is 145 $\mu$K for the $D_1$ and $D_2$ transitions.

The maximum cloud size, i.e. a maximum density $n$, is also limited by the spontaneously emitted photons. A re-irradiated photon by one atoms can be absorbed by another atom. The larger the density the less likely a spontaneously emitted photon will leave the cloud. The re-emitted photon also exert a repulsive force. This is because when one atom emits a photon and another absorbs it, the relative momentum of the atoms increases by $2\hbar k$. The net repulsive force results in expansion of the cloud size and imposes a limit of the atomic density. Generally, the MOT size $L$ scales as $L \propto n^{1/3}$.

### 3.4.1 2D MOT

A 2D MOT is used as a collection chamber for the atoms emitted by the $^{39}$K alkali dispensers. The atoms are confined in two transverse directions into a dense filament. The spatial varying magnetic-field is provided by four permanent magnetic anchored on the corners of the 2D glass chamber.[3] The magnetic field generated by the magnets is shown in Fig.3.4. The field generated is a dipole quadroupole magnetic field, since $|B| = G \cdot r$ where the field gradient is in reference to the centre of the chamber. The gradient, in the

[3]Refer to Appendix D.2 for more.

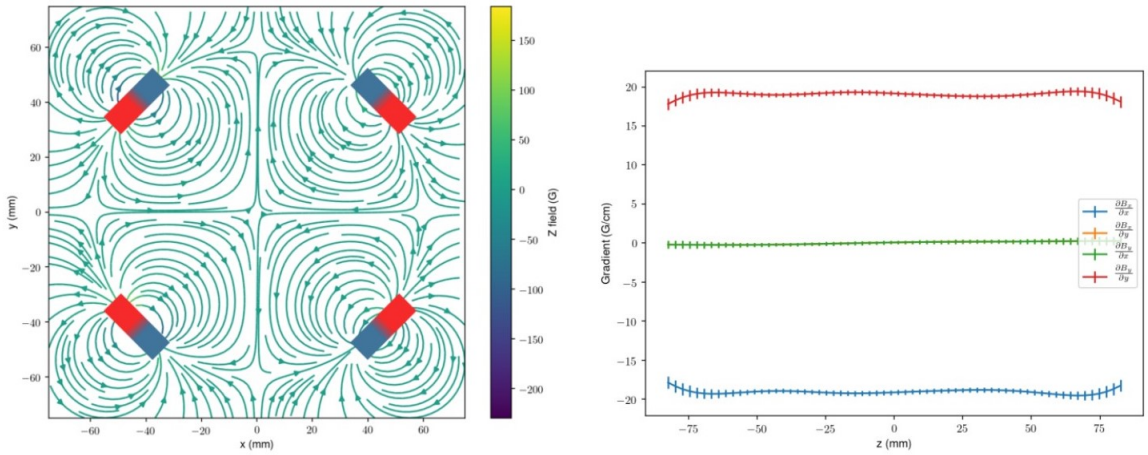


Figure 3.4: Quadroupole magnetic field generated by four permanent magnets in the 2D MOT collection chamber. (a) Simulated magnetic field. (b) The field gradient is $|B| = 17$ G/cm. Taken from Ref.[28]

$\hat{x}$ and $\hat{y}$ directions is $-17$ G/cm and 17 G/cm, respectively. The details of the design of permanent magnets can be found in [28]. .Unlike the quadroupole field generated by an electromagnet, the quadroupole field created by such a configuration of permanent magnets flip sign outside the chamber. In total, 230 mW of total trapping and repumper light is used. The cooling light is $2.5\Gamma$ red-detuned while the repumper was $5\Gamma$ red-detuned. [4]

#### 3.4.1.1 $^{39}$K Dispensers

The potassium dispensers are placed inside in a Y-shaped glass cell. Two natural abundance potassium sources, that is, alkali metal dispenser (AMD) SAES grou are placed inside the glass cell. Currently, of the two branching arms only one of the arm is occupied. The 2D cell heating tape is functional on the four corners of the cell, while the tape on the entrance and exit ends of the cell is not working. The total resistance measured for the heating element is 150 Ω. We have not yet utilized the cell heating but having it turned on has increased the cell temperature by more than $10^oC$ above room temperature approximately.

### 3.4.2 3D MOT

The 3D MOT [5] in the science chamber traps atoms with a spatially-varying scattering force. In total, $\geq$ 40 mW of total trapping and repumper light per beam at 2.4 A TA current [6]. The un-optimized detuning of the 3D MOT beams are the same as the 2D MOT beams;

[4] Note, any power cuts reset the AOM power supply to zero volts output.
[5] Previous generations of students in the $^{39}$K BEC experiment had also obtained a 3D MOT
[6] upto 50 mW per beam can be obtained at 2.8 TA current

the cooling light is 2.5 red-detuned while the repumper is 5 red-detuned. Polarizations fluctuations in each of three axes after P3-630PM-FC fibres have been minimized using HWP and QWP combination.

The magnetic field generated by the coils creates a quadroupole trap. Currently, the coils are cooled with the building water. An Agilent/HP 6464B (0-20 V, 0-20 A 300 W BC) power supply is used for the coils, that is run in the constant voltage regime[7]. The coils are driven at 4 V and 7 A The 3D MOT lifetime is 8.3 seconds with the push beam on.

#### 3.4.2.1 Quadroupole Trap

The anti-Helmholtz configuration of the coils in the 3D MOT chamber provides a Quadroupole magnetic field gradient. The magnetic field due to an anti-Helmholtz pair of coils, results in

$$\mathbf{B}(x,y,z) = -\frac{b}{2}x\hat{x} + -\frac{b}{2}y\hat{y} + (bz + B_0)\hat{z} \tag{3.23}$$

where $a$ is the magnetic field gradient created by the Quadroupole coils, which is typically on the order of few hundred G/cm. Although, the current set-up does not include bias coils, they will be included in the re-designed experiment. The addition of $B_0$ term displaces the centre of symmetry in the Quadroupole gradient.

### 3.4.3 Setting up the new lasers

For the $D_2$ and the $D_2$ optics we have new Toptica seed lasers; DL pro 780_22780 (reffered to as DL1) and DL pro 780_22778 (referred to as DL2), both sharing a Diode Laser Controller (DLC). DL1 and DL2 are pulled to 767 nm and 770 nm, respectively. Both have an elliptical beam shape output of 1:3 mm in size, which are corrected to a gaussian beam shape using telescopes. Their behaviour is characterized in Fig. 3.5 and Fig. 3.6. We are operating DL1 at 218 mA for the 3D MOT [8].

### 3.4.4 Imaging System & Atomic Flux

The atomic flux can be modulated by changing the current at which the dispensers are running. We can monitor the flux by imaging the MOT. We employed laser spectroscopy to image our first 3D MOT.

As a preliminary effort, we imaged our 3D MOT through fluorescence imaging. For a two level system with a ground state $|g\rangle$ and an excited state $|e\rangle$ with natural linewidth $\Gamma$, an atom that has absorbed a resonant photon with frequency $\omega_0$ will re-emit after the

[7] When the overvoltage protection sign (OVP) comes up on the supply when the IGBT circuit is closed and the supply does not switch between constant current (CC) and constant voltage (CV) regimes. It manually switched to a CV source now.

[8] Fast-switching mode is turned on. This stops the DLC from re-adjusting the current at which the DL runs when locking the laser.

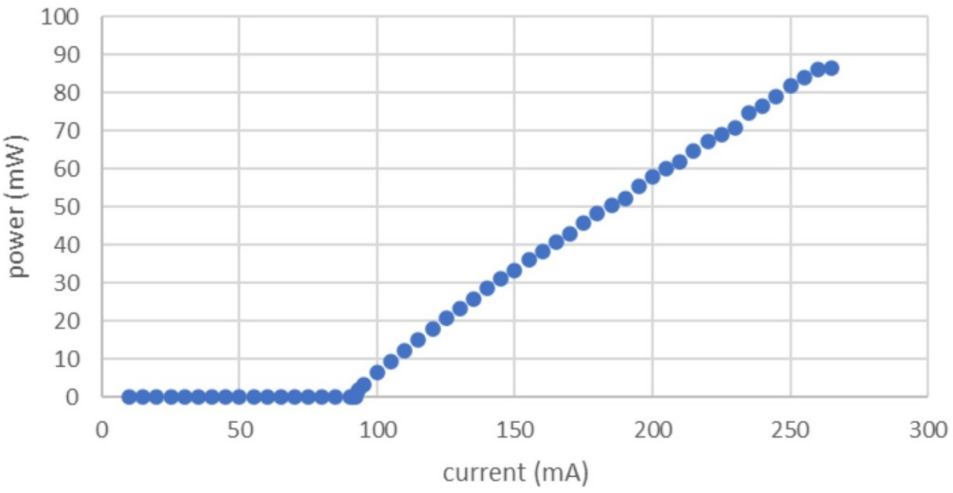


Figure 3.5: Diode Laser (DL2) used for cooling at the $D_2$ transition. Threshold current is 89 mA @ 766.7 nm with maximum power output of 91 mW @263 mA.

lifetime $\tau$ of $|e\rangle$ by spontaneous emission. The photons will be in random directions with equal probability which is observed as fluorescence light. Thus, the atomic density can be extracted by the intensity of the fluorescence detected.

The number of atoms $N$ within the MOT is obtained by

$$N\gamma_{sc} = \frac{4\pi}{\Omega} P_{optical} \tag{3.24}$$

where $P_{optical}$ is the total power and $\Omega$ is the solid angle of captured by the camera and only a part $\Omega/(4\pi)$ of the emitted light lands on the solid angle $\Omega = \pi r^2/d^2$ with $r$ as the size of the MOT and $d$ is the distance between the MOT and camera lens and

$$\gamma_{sc} = \frac{\Gamma}{2} \frac{I/I_{sat}}{1 + I/I_{sat} + (2\Delta/\Gamma)^2} \tag{3.25}$$

is the scattering rate obtained by the product of the number of atoms in the excited $\rho_{ee}$ and the natural linewidth $\Gamma$, $\gamma_{sc} = \Gamma\rho_{ee}$. $I$ is the intensity of the MOT beams, $I_{sat}$ is the saturation intensity and $\Delta$ is the detuning. We employed time-of-flight (TOF) fluorescence to image our atoms. The optical power is attained via calibration of the camera as

$$P_{optical} = c \cdot \frac{0.8\mu W}{0.3 \cdot 10^7} \cdot \frac{113\mu s}{\tau_{exp}} \cdot 1.124^{-G} \tag{3.26}$$

where $c$ is the camera count, that is the intensity obtained by integrating over a region of interest (ROI). The calibration factors are obtained by integrating ROI when shinning a 0.8 $\mu$W beam while setting the exposure time $\tau_{exp} = 113$ $\mu$s and gain $G = 0$ which gives an integrated intensity of $0.3 \cdot 10^7$ arb units. We estimate $10^8$ atoms in the 3D MOT.

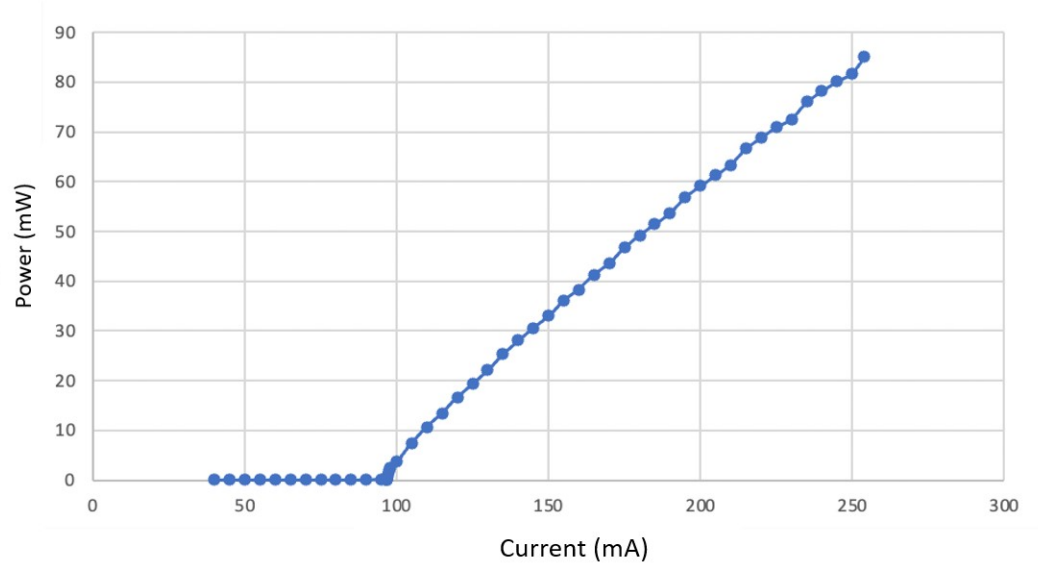


Figure 3.6: Diode Laser (DL2) used for cooling at the $D_1$ transition. Threshold current is 96.8 mA @ 766.9 nm with maximum power output of 85.1mW.

Fluorescence imaging is based on subtraction while absorption imaging is based on division.

The loadtime of the 3D MOT is 8.3 seconds, as reported in Fig. 3.9. By blocking the 2D MOT beams and the push beam we measured the lifetime of the 3D MOT to be 15 sec, approx. Initially, the atoms leave the trap at a rate faster than exponential due to high atomic density leading to greater collisions. But as their density decreases the curve is estimated by an exponential decay and the lifetime is extrapolated. This is lower by a factor of 2 than the previously obtained 30 sec lifetime [38]. The 3D MOT beams had about 30 mW in each beam in our experiment which is well below the saturation intensity of 63 mW at the $D_2$ transition when this measurement was completed. The prior work, had approx. 60 mW in each 3D MOT beam which is double the intensities we have, thus we suspect the lifetime to increase linearly in the high intensity limit upto the saturation intensity.

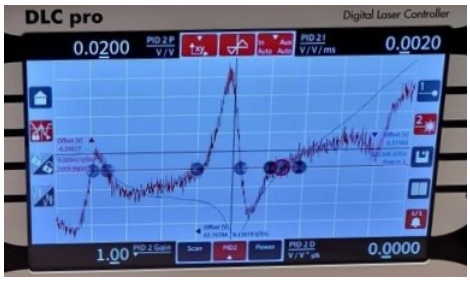


Figure 3.7: Error signal for locking the diode laser on the $D_2$ transition

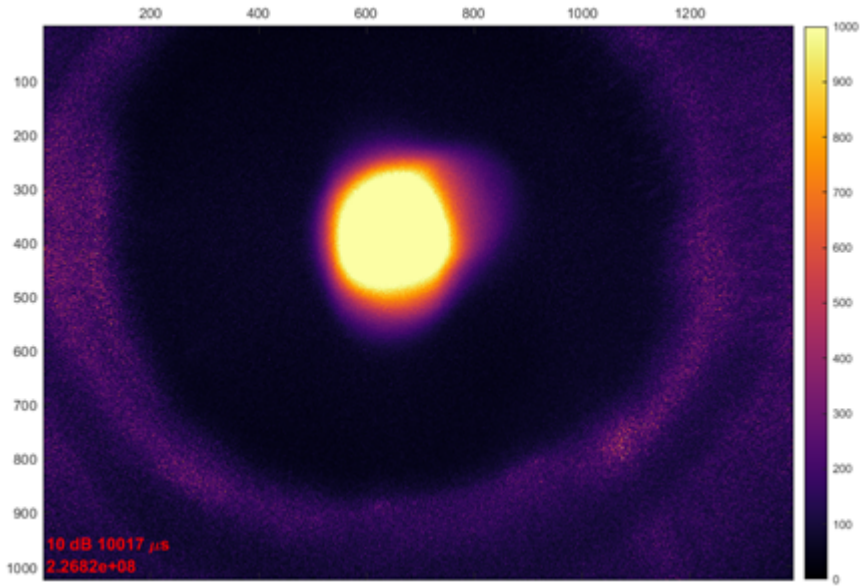


Figure 3.8: Fluorescence image of 3D MOT. The intensity scale is in arb units from 0-1000. The estimated MOT size is $< 0.5$ cm in diameter.

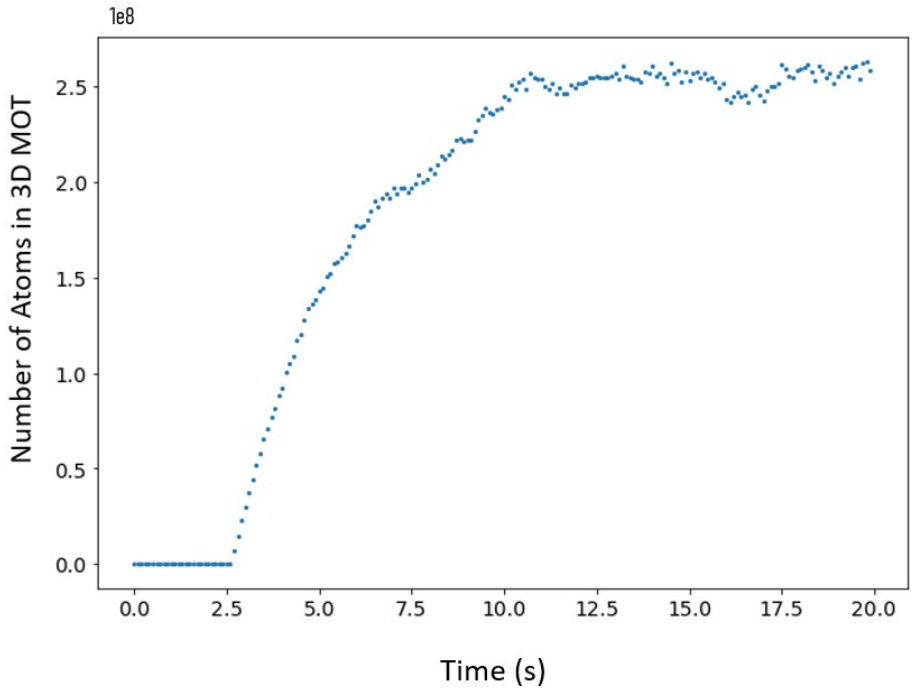


Figure 3.9: Number of atoms in the 3D MOT obtained from fluorescence imaging with exposure time of 25 ms and gain 0. The atom number is retrieved by integrating the total fluorescence in the region of interest.

Time of flight (TOF) thermometry was conducted to measure the temperature of the 3D MOT. This was based on fluorescence imaging to obtain an estimate of the temperature of the cloud. The all $D_2$ beams are switched off first, then the magnetic field using the Adwin, so that that the atoms balistically expand within a few ms. Then, the expanded cloud is imaged by shinning resonant light beam, that is the 3D trap and repump DP AOM is zero-detuned [9]. The temperature of the initial cloud $\sigma_0$ is related to the cloud size

$$\sigma(t) = \sqrt{\sigma_0^2 + \sigma_v^2 t^2} \tag{3.27}$$

where $\sigma_v = \frac{k_B T}{m}$, $T$ is the cloud temperature and $t$ is the expansion time elapsed after dropping the cloud. The temperature of the cloud is 4.4 mK as illustrated by Fig.3.10.

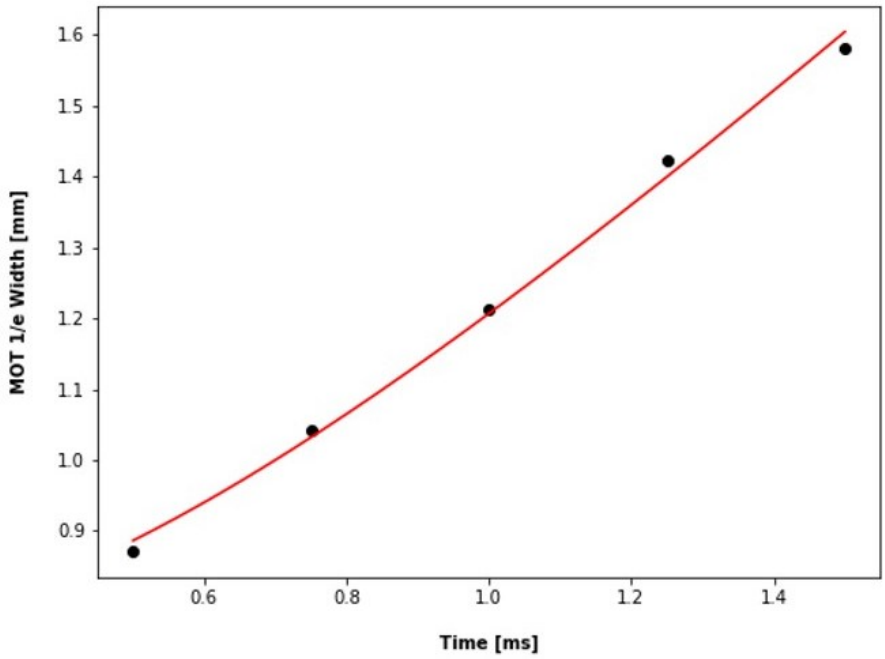


Figure 3.10: Time of flight fluorescence thermometry, with 3D MOT cloud size vs expansion time elapsed. Temperature is the 3D MOT is obtained by fitting to equation 3.27.

## 3.5 Sub-doppler Cooling: Gray Molasses

Gray molasses cooling mechanism is a sub-doppler cooling process that combines two techniques - Sisyphus cooling and Velocity Selective Coherent Population Trapping (VSCPT) [43, 46, 2]. This cooling mechanism does not work for a two level system, but rather, it requires a $\Lambda-$system wherein the internal states of the atom are an excited state $|e\rangle$ and it

[9] Future iterations TOF imaging will include addition of a shutter to block the push beam.

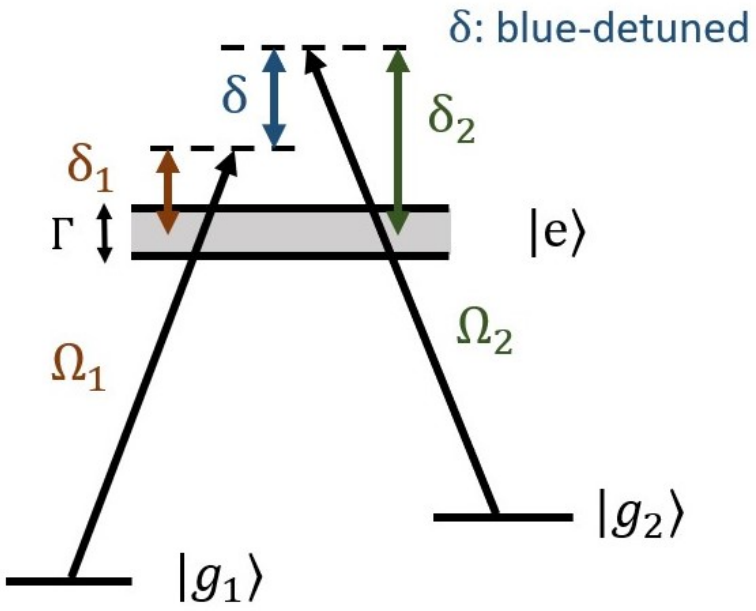


Figure 3.11: Λ-system used for Gray Molasses cooling, with two ground states $|g_1\rangle$ and $|g_2\rangle$ that are coupled to an excited state $|e\rangle$ with Rabi frequencies $\Omega_1$ and $\Omega_2$ and detuninigs $\delta$ and $\delta_2$ , respectively.Gray molasses is a two-photon process with two-photon linewidths of an order of magnitude less than the natural linewidth of the transition $\Gamma$. Adapted from [20].

has two ground states $|g_1\rangle$ and $|g_2\rangle$, as shown in Fig.3.11. The Hamiltonian of a free atom constitutes of its kinetic energy $\mathcal{H}_{kin}$ and internal energies term $\mathcal{H}_0$.

$$\mathcal{H} = \mathcal{H}_{kin} + \mathcal{H}_0 \tag{3.28}$$

with

$$\mathcal{H}_{kin} = \frac{\mathbf{p^2}}{2m}$$
$$\mathcal{H}_0 = \hbar\omega_e \left|e\right\rangle \left\langle e\right|$$

where $\omega_e$ is the energy of the excited states while the energies of ground states are arbitrarily chosen as $E_{g1} = E_{g2} = 0$. $\Omega_1$ and $\Omega_2$ give the Rabi pulses of the bichromatic laser. Such that, the coupling term between the atom and the field $_{AL}$ in the rotating-wave approximation (RWA) is given by

$$V_{AL} = \left(\frac{\hbar\Omega_1}{2}\left|e\right\rangle\left\langle g_1\right| + \frac{\hbar\Omega_2}{2}\left|e\right\rangle\left\langle g_2\right|\right) e^{-i\omega t} \tag{3.29}$$

Both beams are linearly polarized such that the atoms experience a spatially dependent polarization gradient [10] or a spatially varying light intensity modulation, as shown in Fig.3.12.

The Raman detuning between the two laser beams [11] is $\delta = \delta_2 - \delta_1$ where $\delta_1$ and $\delta_2$ are the detunings of each of the laser fields that couples $|g_1\rangle$ and $|g_2\rangle$ to $|e\rangle$, respectively. At the Raman resonance condition $\delta = 0$, that is $\delta_2 = \delta_1 = \Delta$, there exists a linear combination of the two ground states $|g_1\rangle$ and $|g_2\rangle$ which does not couple to the laser field

$$|NC\rangle = \frac{1}{\sqrt{\Omega_1^2 + \Omega_2^2}} \left(\Omega_2 |g_1\rangle - \Omega_1 |g_2\rangle\right) \tag{3.30}$$

This is the non-coupling $|NC\rangle$, i.e. dark state. In the case of $^{39}$K, an example dark state is $\left(|F = 1, m_F = -1\rangle - |F = 2, m_F = -1\rangle\right)/\sqrt{2}$. One can prove that this linear superposition is the dark state by applying the coupling Hamiltonian $V_{AL}$. Thereby, $\langle e| V_{AL} |NC\rangle$ vanishes.

However, the state orthogonal to $|NC\rangle$, i.e. the bright state is optically accessible such that

$$\langle e| V_{AL} |C\rangle = \frac{\hbar}{2}\sqrt{\Omega} e^{-i\omega t} \tag{3.31}$$

The coupling probability between $|C\rangle$ and $|NC\rangle$ can be obtained from first order perturbation theory as:

$$P_{|NC\rangle \to |C\rangle} = 2\left(\frac{\Omega_1 \Omega_2}{\Omega_1^2 + \Omega_2^2} k \frac{p}{m}\right)^2 \delta_1 \left(\frac{\delta_1}{\Omega_1^2 + \Omega_2^2}\right) \quad \propto v_{atom}^2 \tag{3.32}$$

Evidently, there occurs strong coupling at high velocities of the atom $v_{atom}$ and at lower light shift of the bright state, in the form of Rabi frequency [20]. Unlike a MOT, GM is a two-photon process. Gray molasses cooling is enhanced by velocity-dependent dark state generated via two-photon resonances. So as long as the velocity class of the atoms is $|v_{atom}| > 0$, the VSCPT mechanism ensures that the atom is included in the cooling process until $v_{atom} = 0$. Neither $|NC\rangle$ nor $|C\rangle$ are eigenstates of the momentum operator, thus there is non-zero overlap between the two states. That is, the dark state can leak into the bright states proportionally to the non-zero velocity of the atoms and hence they are motionally coupled to one another. The blue-detuning of the laser beams establishes that the coupling is more likely at the bottom of the spatially-dependent potential seen by the coupling state $|C\rangle$.

## 3.6 Optical Dipole Traps

We will use high-intensity, far-detuned beams of light to generate optical dipole potentials for the atoms. The dipole force from a laser beam results from the interaction between the

[10] Gray molasses is extremely sensitive to any extraneous magnetic field due to the narrow functionally cooling width of the two-photon detuning. We are currently implementing bias coils to compensate the earth magnetic field, and stray fields due to the 2D MOT permanent magnets and the ion pump.

[11] 400mW of total power from the $D_1$ optics at 2.4 A TA current is available

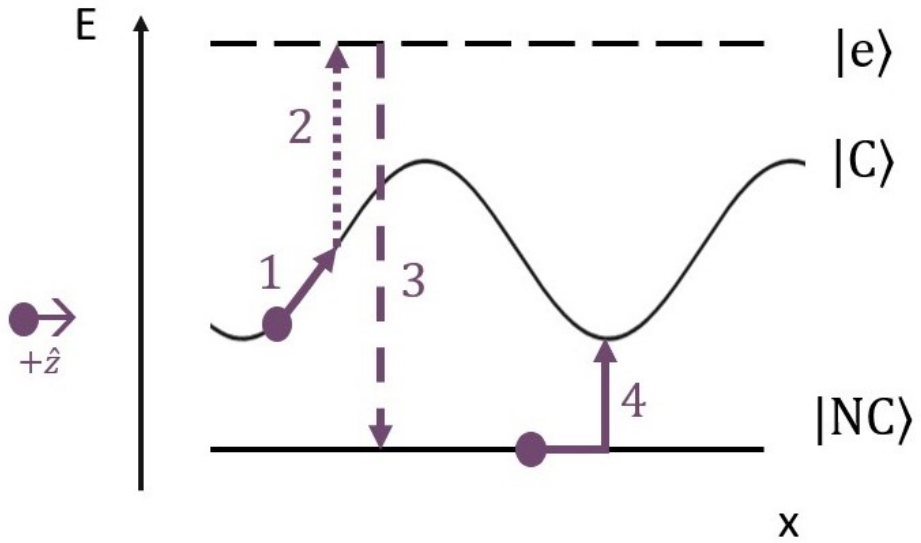


Figure 3.12: Gray Molasses (GM) cooling mechanism. An atom in the coupling state $|C\rangle$ propagating in the $+\hat{z}$ direction encounters a spatially-varying potential and climbs up the energy hill, in step 1. The $|C\rangle$ state is optically coupled to an excited state $|e\rangle$ and the atom gets optically pumped, in step 2. Spontaneous emission from $|e\rangle$ preferentially leaves the atoms in the non-coupling $|NC\rangle$ state, as shown in step 3, which completes the sisyphus cooling cycle. In the final step 4, the atom transitions from $|NC\rangle \rightarrow |C\rangle$ due to the matrix element given in equation 3.32 resulting from VSCPT mechanism. Adapted from [20].

electromagnetic field and the induced dipole moment of the atoms. This interaction gives a potential that scales as $\Delta^{-1}$ with the detuning and as $\Delta^{-2}$ with the scattering rate. For large detunings, the dipole force from the beams form a conservative trap for the atoms during the lifetime of the atomic cloud. In the rotating-wave approximation (RWA), the ligh-matter Hamiltonian is of the form

$$H_{int}^{RWA} = \frac{\hbar}{2}\begin{bmatrix} -\delta & \Omega_R \\ \Omega & \delta \end{bmatrix} \tag{3.33}$$

where the Rabi frequency $\Omega_R = -\left\langle \hat{\mathbf{d}} \cdot \mathbf{E} \right\rangle$ and $\delta$ is the detuning. The eigenenergies $E_\pm$ this dipole interaction Hamiltonian are $E_\pm = \sqrt{\delta^2 + \Omega_R^2}$. Thus, the energy of a state is proportional to the Rabi frequency $\Omega_R$. Since the energy of a state $E_\pm \propto \Omega_R \propto |\mathbf{E}|^2 \propto I(x, y, z)$, the dipole trap will form a conservative attractive or repulsive trap depending on the detuning of the dipole trap beams, red or blue-detuned, respectively. For a red-detuned 1064 nm beam the atom atoms experience an attractive potential towards regions of highest intensity. Following the trapping of atoms, evaporation is to be realized in a crossed optical dipole trap (ODT).

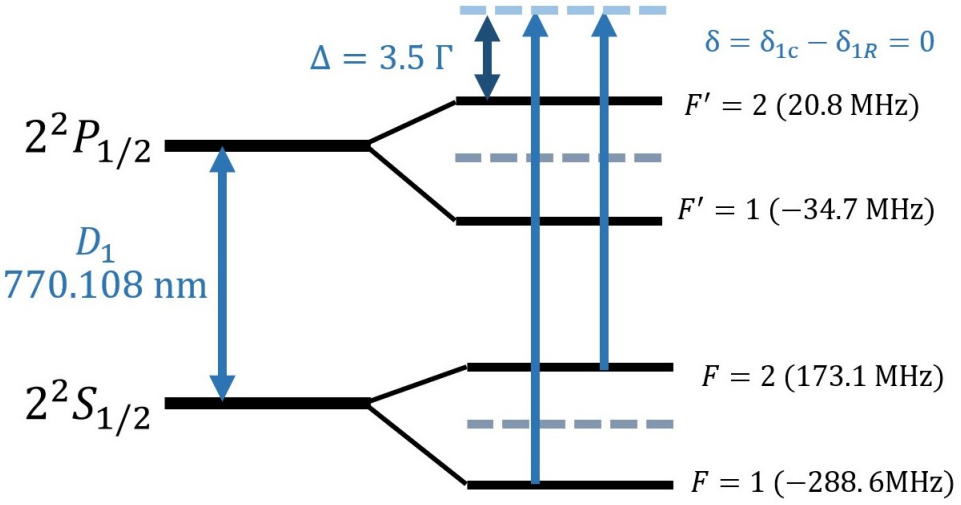


Figure 3.13: Atomic transition at 770 nm used in $D_1$ cooling of $^{39}$K. The $|F = 1\rangle$ and $|F = 2\rangle$ form the two ground states in Λ-enhanced gray molasses. The beams are blue-detuned relative to the excited state. Adapted from [43, 20].

## 3.7 Evaporative Cooling

After optical molasses, the atoms have a temperature below the Doppler limit yet greater than the recoil temperature. The recoil temperature of $^{39}$K is $0.41\mu$K at the $D_1$ transition. However, to reach degeneracy and achieve a BEC, the momentum distribution of the cloud must be reduced to the nK scale. This can be attained via *evaporative cooling*. At the beginning of evaporation, the atoms have a energy distribution characterized by the Boltzmann statistics

$$N(E) = N_0 e^{-E/k_B T} \tag{3.34}$$

at some temperature T. By decreasing the trap depth, atoms with energies greater than some cut-off energy $E > E_{cut}$ escape the trap. For typical fractions of $\eta = 3-6$, the cut-off energy is $E_{cut} = \eta k_B T$. The highest kinetic energy fraction takes away the energy from the cloud, leaving behind a colder ensemble following re-thermalization. The thermalization rate goes as $\sim n^2$, where $n$ is the density of atoms. If evaporative cooling is carried out at a rate faster than the atoms can re-thermalize, then the process simplifies to that of non-interacting gas, where no collisions occur such that colder atoms are not produced; they are just selected out from the others.

Since the atomic density increases, as the colder atoms sink at the bottom of a harmonic trap, the phase space density following evaporation increases so that quantum statistics rule over. Although, there is no fundamental limit to evaporative cooling, practical reasons set a lower bound. Below the critical phase-space, discussed in Section 2.1, a bosonic ensemble undergoes a phase transition to a Bose condensate.

## 3.8 States to be trapped

Stern and Gerlach, notably, used a strong inhomogeneous magnetic field to separate spins in a thermal atomic beam. They used the magnetic forced exerted on the atoms as they traverse through the magnetic field region. The atoms have a magnetic dipole which precesses in a magnetic field due to the torque that the magnetic field exerts on the dipole. Magnetic trapping and transport of atoms is based on the interaction between the magnetic dipole $\boldsymbol{\mu}$ of an atom and the magnetic field. The energy of a magnetic dipole $\boldsymbol{\mu}$ in a field has the form

$$E = -\boldsymbol{\mu} \cdot \mathbf{B} \tag{3.35}$$

which for an atom in state $|JFm_F\rangle$ corresponds to a Zeeman energy shift which depends only on the magnitude of the magnetic field

$$E_{Zeeman} = g_F \mu_B m_F |B| \tag{3.36}$$

where $g_F$ is the state-dependent Landé $g-$factor and $\mu_B$ ($\approx 1.4$ MHz/Gausss) is the Bohr magneton. The force exerted on the atoms is then

$$\mathbf{F} = -\nabla U = -g_F \mu_B m_F B \tag{3.37}$$

To perform magnetic transport during the experiment the states to be used must be magnetic trappable within quadroupole magnetic field. The $|F, m_F\rangle = |1, 0\rangle$ state has a vanishing first-order Zeeman shift $\Delta E_{Zeeman} = 0$, although the second-order shift is non-zero. So, unlike the $|1, -1\rangle$ state, it is not magnetically trappable upto first-order in magnetic field.

Any states with $g_F \mu_F > 0$ will lower their energy by moving towards a minimum in magnetic field, as seen from 3.37, and hence they are magnetically trapable. Such state are known as *low-field seeking* states. For $^{39}$K, the $g_F$ factors are $g_{F=1} = -1/2$ and $g_{F=2} = 1/2$. So, $|1, -1\rangle$, $|2, 1\rangle$ and $|2, 2\rangle$ are trappable states.

# Chapter 4

# Progress towards an Ultracold Cloud

We consider the design of the new BEC experiment to be built. Maintaining an ultra-high vacuum is critical for obtaining a BEC. We will reach degeneracy in an optial dipole trap. The current expeimental set-up will be updated. Here, we discuss the basic physics of alkali vapour used to load a trap, the optical dipole trap to be used to reach degeneracy and the other design considerations.

## 4.1 Vacuum System

In our experiment, we load the 2D MOT from a background vapour of $^{39}$K atoms. This background vapour containing other non-alkali atoms as well, such as $N_2$, $CO_2$, Ar, $H_2$, etc. gases. The vapour pressure of the atom in interest is adjustable via modulating the temperature of the alkali dispensers (from SAES) that is the attached to the 2D MOT cell.

In order to get the atoms into a trapped state, the background vapour pressure needs to be on the order of $10^{-9}$ Torr or lower. Obtaining an accurate estimate of the vapour pressure in ultra-high vacuum conditions is non-trivial. The vapour pressure for $^{39}$K is estimated as [53]:

$$\log P[\text{Torr}] = 7.9667 - \frac{4646}{T} \tag{4.1}$$

for 298K < T < $T_m$.

An accurate measurement of the vapour pressure in the chamber can be obtained from an absorption measurement using Beer's law: $n\sigma l = \log 1 - A$; where $l$ is the path length and the absorption cross-section for potassium is $\sigma = 2.7 * 10^{-9}$ cm$^2$ for $\sigma^{\pm}$. Using the ideal gas law, the pressure can be estimated as $P = nk_BT/V$. However, absorption spectroscopy is not current set up in our system. For more details on vacuum theory, refer to Appendix A.

### 4.1.1 Experimental System

The current configuration of the vacuum system was designed by Bernie Hsu and it is reported in detail in Ref[24]. The current vaccum system contains two chambers: a 2D MOT chamber and the 3D MOT chamber where UHV is achieved and in which the rest of the experimental cycle takes place. The link between the two chambers is made via a tube of 1.5 mm in diameter. Atoms are ejected from a potassium dispenser (...SAES) and collected into the 2D MOT chamber. The 2D chamber is used to collect atoms from the source and as a molasses stage for subsequent capturing and cooling of atoms in the 3D MOT chamber. The science (3D MOT) chamber is where the rest of the experimental cycle is planned to occur.

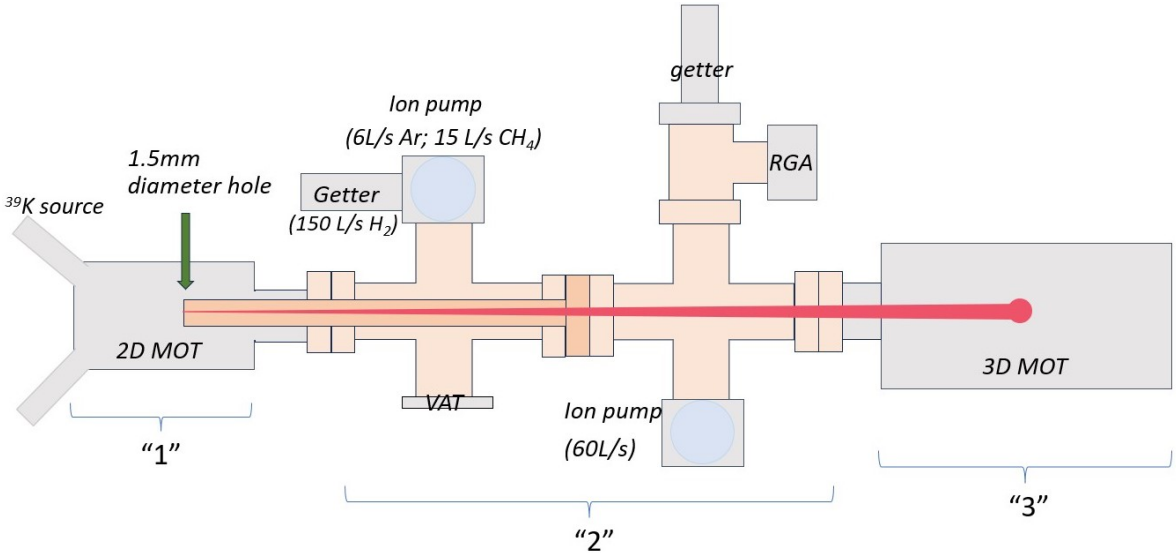


Figure 4.1: Schematic of the proposed vacuum system.

#### 4.1.1.1 Proposed Vacuum System

The present experimental system lacks an active pumping element for the 2D MOT chamber. The background vapour pressure in the first chamber is estimated to be $10^3$ times higher than in the science chamber. However, we do not have a pump controller attached this chamber so we do not have a measure of the pressure inside the chamber, only a relative estimate. Additionally, the science chamber is an octagonal steel chamber where optical access is limited. Thus, here we consider a re-designing of the vacuum system to accommodate for the scientific goals of this experiment.

There are four criteria that need to be satisfied in the re-designing of the vacuum system. First, there must be *isolation* between the various chambers in the system such that the background pressure differs by $10^{-3}$ orders in various chamber, discussed further in 4.1.1.2. Second, the 2D MOT chamber is deprived of active pumping, so there needs to be

*adequate pumping* of the both the collection and the science chambers, that is elaborated in 4.1.1.3. Third, for large enough atom numbers ($10^9$ or more atoms) in the 3D MOT, a *high solid angle* of the 3D MOT is necessary which is examined in A.1.1. Forth, the final experimental system demands a *large optical access*. These constraints are satisfied by the proposed vacuum system shown in Fig.4.1 and are further elaborated below.

#### 4.1.1.2 System Conductance

The conductance of a component $C$ is given by the conductance $C_A$ [1] of its aperture times a transmission probability $\alpha$, $C = \alpha C_A$. Transmission probabilities are calculated using statistical MonteCarlo methods which can be applied to complicated shapes, such a conical cross-sections [31]. The maximum pumping speed of a high vacuum pump cannot be larger than the conductance of its aperture [2].

From the residual gas analyzer (RGA) scans, the partial pressure of $H_2$ gas dominates the science chamber, followed by $N_2$. $H_2$ is greater than $10^{-9}$ Torr, which is an order of magnitude greater than the partial pressure of the rest of the gases.

Differential pumping of the order of $10^{-3}$ and a final ultrahigh vaccum level in science chamber $10^{-11}$ Torr is required to minimize losses from the MOT trap due to collisions from the background vapour. The conductance of the science chamber is calculated to be 27 L/s for the current geometry [34]. With the system depicted in Fig.4.1, the overall conductance from the 3D MOT to the 60 L/s ion pump is 13.5 L/s [3] if the current conical reducers are kept. By adding the pump in this arrangement, this conductance sets maximum effective pumping speed achievable.

To reach ultrahigh vacuum, the 2D collection chamber and the 3D MOT chamber must be isolated from each other. The two chambers are linked via a series of a crosses that are separated by a differential pumping tube of 1.5 mm in diameter. The effective conductance between the two must, therefore, be low. In the configuration illustrated in Fig.4.1, the effective conductance is 0.054 L/s [4].

#### 4.1.1.3 Pumping of the System

The ultrahigh vacuum would be maintained thanks to the two ion pumps, one in each of the collection and science chambers in the new vacuum system.

Traditionally, sputter ion pumps, which are used as the main pump, fulfil the pumping speed requirements and compact getters are used to boost the $H_2$ pumping. In the proposed vacuum design, NEXTorr Z 100 pump [5] combines a compact getter element integrated with a small ion pump. The getter elements acts as the main pump and provides

[1] For apertures, the conductance can be estimated as $C = 9.3D^2$ Litre/s, diameter $D$ in cm

[2] For cylindrical tubes, $C = 12.4\frac{D^3}{L}$ Litre/s, diameter $D$ and length $L$ in cm

[3] Calculated for DN40CF flange size, which is available for a standard rectangular glass cell from ColdQuanta with dimension of 2 cm × 2 cm× 60 cm.

[4] Calculated for DN40CF four way crosses available from Kurt J. Lesker.

[5] NEXTorr Z 100 comes with CF35 flange size

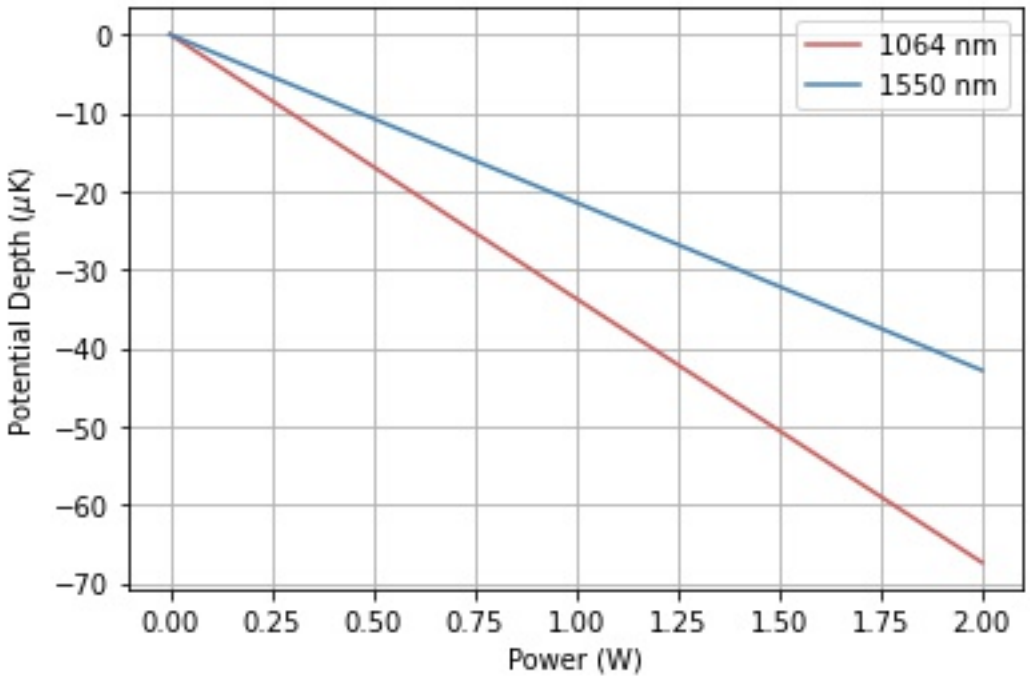


Figure 4.2: Polarizability of 1064 nm VS 1550 nm. Negative potential amounts to an attractive trap. At 2 W, the 1064 nm trap is deeper than the 1550 nm.

the predominant pumping speed (150 L/s) wihle the ion pump removes the noble gases, primarily Ar (6 L/s) and $CH_4$ (15 L/s). We currently have is a single 60L/s Ion Pump (Duniway, RVA-060-DD.) on the opposite end of the of the science chamber to the 2D MOT. A residual gas analyzer (RGA from Stanford Research System - SRS) is also placed in the second-cross which is a proxy for the partial pressure of the various gases.

Ion pumps, as their name suggests, ionize the gas and then employs a strong electrical potential to absorb the atoms on an electrode. The cathode is chemically active and typically composed of titanium. Ionization works by sputtering the atoms with a getter material. Typically, turbomolecular and ion pumps are inefficient at pumping hydrogen.

Non-evaporable getter pumps (NEG) contain a compact getter material that is porous at the atomic level. As such, it can take up large amounts of gas. Typically, the getter material is made of zirconium-aluminum alloys in the form of strips. On the surface of the getter material, the gas molecules are chemisorbed and physisorbed diffuse rapidly inside the material thereby making place for more gas molecules crushing on the surface. Physisorption involves formation of weak bonds due to van der Waals forces (¡ 10 kcal/mol). NEG pumps are able to reversibly sorp by chemical reactions on the material surface, where hydrogen and its isotopes dissociates and diffuse in the getter materil forming a solid solution. Hydrogen does not react to form a chemical compound, rather it dissolves in the bulk of the getter forming a solid solution. Getters do not pump noble gases as they are not chemically reactive. Other gases that are pumped by the getter include CO,

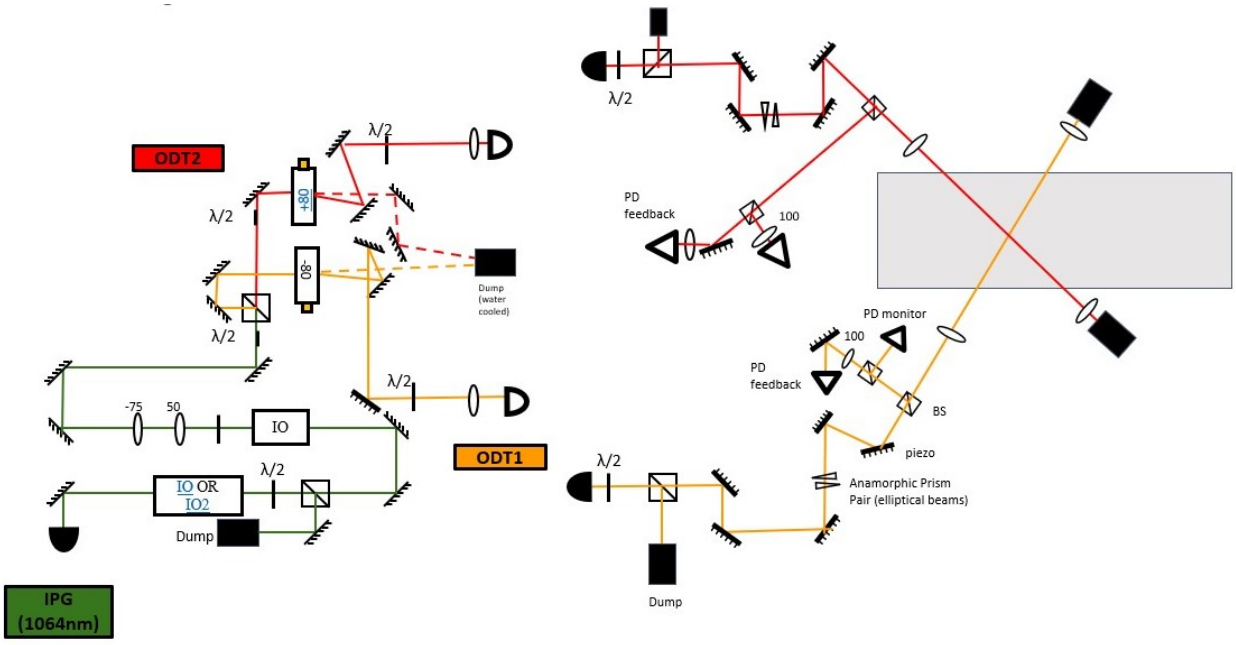


Figure 4.3: Schematic of optical system for Optical Dipole Trap (ODT). A 1064 nm IPG laser will be used and the beam will be split in two paths (red and yellow). The 80 MHz AOM will be remotely controlled. The beams will be fiber coupled to the science table where they will be stabilized using two photodiodes; one for monitoring and one for the feedback loop. An amorphic prism pair will be used for mode matching with the optical lattice.

$H_2O$, $CO_2$, $O_2$ and $N_2$. They also contain a heating element that heats up the getter material to a temperature depending on the gas to be pumped. Saturated getter lattice can be regenerated, i.e. activated, by setting the heating element to higher temperatures. Activation involves heating *under vacuum* at typical activation temperatures of 400-500$^o$C. for approximately an hour. Getters can sorb gases after activation without requring power.

#### 4.1.1.4 Science Chamber

Optical access is ensured the rectangular glass cell. The design of the glass cell is proposed by Nick Mantella. Here, we inform the reader of the decision / design considerations which are necessary to gain insight to the experimental apparatus. The design considerations go hand-in-hand with the scientific goals this new generation experiment is aimed at are further discussed in Appendix B.

## 4.2 Optical Dipole Trap (ODT)

Optical Dipole Trap are far-detuned beams that create an conservative trap where atoms are attracted to the highest intensity region, as described in Section 3.6. To avoid forming an optical lattice, the lasers used for dipole trap are broadband [55]. Two possibilities for a dipole trap for $^{39}$K were either 1064 nm or 1550 nm. The dipole potential for large detunings and negligible saturation is given by [47]

$$U_{dip}(\mathbf{r}) = -\frac{3\pi c^2}{2\omega_0}\left(\frac{\Gamma}{\omega_0 - \omega} + \frac{\Gamma}{\omega_0 + \omega}\right) I(\mathbf{r}) \tag{4.2}$$

where $I(\mathbf{r})$ is the intensity of the beam. Upon characterization of the atomic polarizability [6] of $^{39}$K at these two wavelengths, we decided on 1064 nm wavelength. For instance, for a trap depth of -40$\mu$K, the beam power required for 2 W for 1550 nm while 1.25 W for 1064 nm, as shown in Fig.4.2. This is calculated for peak laser intensity $I_0 = 2P/(\pi * \omega_0^2)$.

We will use an IPG YLR-50-1064-LP, 50W CW linearly polarized 1064nm Ytterbium Fiber Laser that has a 19" air cooled rack mount and a terminated 5 m fiber. A proposed optical path for the dipole trap optics is given in Fig.4.3, for a beam diameter of $\sim$ 3.6 mm.

[6] Useful polarizability data is also available here: https://www1.udel.edu/atom/K1Polarizability.html

# Chapter 5

# Future Directions

The $^{39}$K BEC experiment has impart budded out of the $^{87}$Rb BEC experiment in the Steinberg group in that it is directed to explore the interactions of matterwaves with tailored potentials. It targets to probe interacting condensates in diffraction limited potentials. As discussed in Section 1.2, the atomic species of $^{39}$K has versatile scattering properties at accessible of tuning interactions, contrary to $^{87}$Rb. The tunability of interaction length in $^{39}$K makes it highly desirable for applications in interacting BECs. Here, we discuss some of future experiments of study. The final experimental apparatus will contain a 3D optical lattice as well but the state of this aspect is too premature to discuss here.

## 5.1 Matter-Waves

In an experiment led by David Spierings, the $^{87}$Rb condensate was aimed to determine the *reflection* times of the BEC from a barrier region, rather than the tunneling times [54]. Reflection of a BEC from a barrier is not limited to the surface of the barrier, but it is exponential supressed in the centre of the barrier [49, 48]. The total time spent inside the barrier by the reflected and transmitted wavepacket is same [40]. Interestingly, it was observed that the reflected wavepacket which carried information about the larmor times [4] interacts with the incoming wavepacket, leading to spin waves. Thus, the tunability of interactions using the Feshbach resonances in $^{39}$K would allow for a meticulate study of reflected portion from the barrier region or studying interaction-driven spin rotations in the reflected and the transmitted wavepackets.

### 5.1.1 Atomic Fabry-Perot

A matter-wave Fabry Perot is an atomic equivalent of the regular optical Fabry-Perot (FP) where the role of matter and photons is switched. The cavity is created by a repulsive double barrier while the wave will be generated by a $^{39}$K BEC. Simlar to an optical FP, a matterwave FP can be characterized by its free spectral range and the finesse. The free spectral range describes the frequency spacing between resonances determined by the

cavity length. The finesse characterizes the width of the resonances which is dictated by the reflectivity of the cavity (frequency dependence of waves in optical FP is often neglected).

The tunneling probability

For the matter-wave analogue, the reflective of the BEC depends on its incident velocity[1]. A condensate with higher kinetic energy impringing on the barrier beam has lower effective reflectivity and hence a broadened associated resonance, as seen in Fig. 5.1. The resonance width $\Delta v$ has a corresponding temperature given by

$$T = \frac{m(\Delta v)^2}{k_B} \tag{5.1}$$

where $m$ is the mass and $k_B$ is the Boltzmann constant. A BEC hitting the barrier at a lower velocity has lower tunneling probability. In momentum space, when the velocity width of the incident wavepacket is greater than the width of the resonances, the resonances are blurred out.

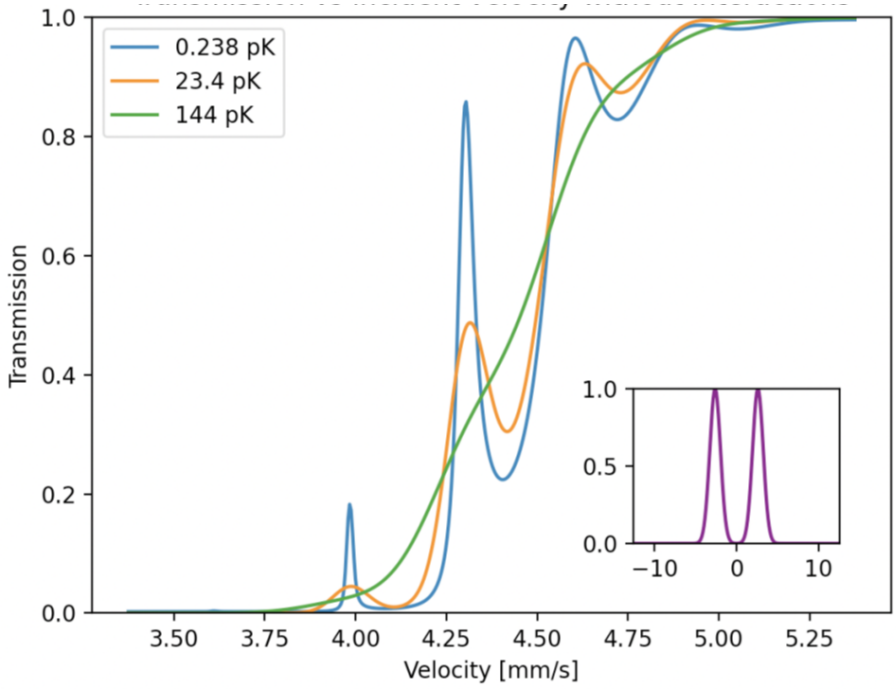


Figure 5.1: GPE simulation for a non-interacting BEC at different temperatures. Taken from [29].

The existence of interactions within a BEC, introduces a non-linear term in the Schrodinger equation, known as the pseudopotential. The interaction term, introduced in 2.7. The location of the resonances within the cavity depend on the potential inside the cavity. If the BEC interacting within the cavity, the interactions modify the potential such that the rest

[1]In the matter-wave case, it is constructive to refer to velocity widths, rather than frequencies. The resonance width (finesse) can be expressed in terms of a velocity width as well.

of the condensate is no longer resonant which smooths out the resonance peaks, as shown in Fig.5.2. Increasing the strength of the coupling constant $g$ results in more dramatic wash-out of the peaks. An attempt to conduct the atomic FP experiment resulted on the background transmission being observed through the double-barrier with no evidence of resonances. Since the $^{87}$Rb BEC is an interacting BEC, the potential created by the interactions altered the potential within the cavity. As well as, the experiment lacked the ability to tune the cavity length, by means of modifying the length between the double-barrier since it was generated using a piece of glass at an angle that such that the $\pi$ phase shift was introduced to half of beam. However, using SLMs in the new experiment would enable to

Evidently, controlling interactions using the magnetic Feshbach resonances in $^{39}$K would impart circumvent or at least significantly decrease the interaction strength within a BEC close to a zero-crossing of the scattering length. If practically possible, the Delta-Kick cooling would also allow for reaching low enough velocity width, that is an effective temperature of $< 1$ nK, on the scale of a few hundreds pK.

Another future expedition could involve generating a two consecutive double-barriers, where the length of cavity generated by the second double-barrier is some integer multiple of the first one. Resonances that are blurred out for an ultracold wavepacket ($\approx 1nK$ width) in the first double-barrier will become visible in the second, even at temperatures higher than few hundred $pK$. This is because the first one would filter out the velocity distritbution that is resonant to the cavity which is picked up by the second.

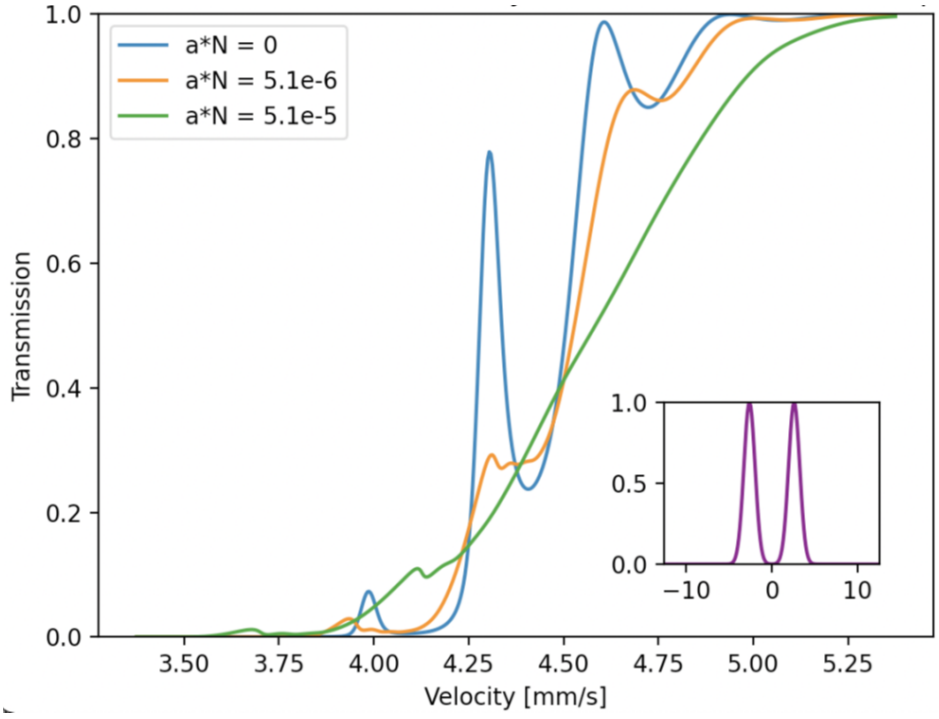


Figure 5.2: GPE simulation at different interaction strength. Taken from [29].

#### 5.1.1.1 Generating a Double-Barrier

In the future experiments, blue-detuned double barries will be generated using a liquid-crystal spatial light modulator (SLM). The repulsive potential will be generated by a 405 nm beam. For an incident gaussian beam, applying a $\pi$ phase shift to half of the beam results in a double-barrier in the fourier plane. Such a phase mask can be applied by an SLM. A $\pi$ phase shift to half of the beam effectively creates a Hermite-Gaussian $\mathrm{TEM}_0 1$ mode due to the phase discontinuity in the centre of the beam that gives an interface in the Fourier plane. SLMs have liquid crystal in each pixel, in which the orientation of molecules is changed by applying a variable voltage. This changes the index of refraction in each pixel based on the applied voltage [2].

#### 5.1.1.2 Delta-kick cooling

The transition to BEC occurs below the critical temperature, that is on the order $\mathcal{O}$(nK). However, in order to resolve the resonance peaks in a matterwave Fabry-Perot, the width of the resonances must be on the scale of the velocity width of the incident BEC. The finite velocity width, given in 5.1, is directly determined by the temperature of the condensate. Evidently, from simulations shows in Fig. 5.1, this occurs at the sub-$nK$ scale. Thus, another mechanism, known as delta-kick cooling [3], must be carried out to reduce the width broadband wavepacket to the $pK$ scale [15].

Briefly, the priciple of delta-kick cooling in phase-space is as follows. Initially, the atomic cloud is confined in some region $\Delta x_0$ the wigner function of which is a gaussian in the ideal case. The trap is then turned-off to let free expansion of the cloud, during which position and momentum of the atoms are correlated. A momentum kick is impringed by the linear force generated from an harmonic trap. The final temperature attainable is limited by the ratio of sizes of the initial $x_0$ and final $x_f$ clouds as

$$\frac{T_f}{T_0} = \left(\frac{\Delta x_0}{\Delta x_f}\right)^2 \tag{5.2}$$

where $T_0$ is the initial cloud temperature. Contrary to evaporative cooling, DKC preserves phase-space density. The temperature decreases at the expense of a larger final cloud size.

The presence of interactions reduces the efficiency of DKC. Interacting particles approximated by the Thomas-Fermi distribution. It takes some time for the interaction energy to tranform into kinetic energy of atoms before the position-momentum correlations come in.

A waveguide beam will be used to encapsulated the BEC. To avoid forming an optical lattice with the glass cell, the waveguide beam is broadband. Additionally, for a more focused as waist size decreases, as in the case of the barrier beams which will be on the

[2] Given an initial Gaussian beam profile, the phase mask is obtained by the Gerchberg-Saxton (GS) algorithm. A modified GS algorithm, known as Mixed Region Amplitude Freedom (MRAF) corrects for speckling.

[3] also known as, matter-wave lensing

order of $\mathcal{O}(10\mu\text{m})$ [4], the Rayleigh range $R$ increases ($R = \pi\omega_0/\lambda$) to conserve momentum. Thereby, the waist of the waveguide beam must also be on the same order to avoid variations in the barrier width seen by the BEC. DKC will be performed only in 1D, in the longitudinal direction of the waveguide.

[4] Beam waist up to a sub-$nm$ precession can be measured using the knife-edge technique [39]

# Appendix A

# Vaccum Theory

Angular distributions:

In HV and UHV (.. torr), the atoms obey the molecular flow regime. In this regime, due to the low atomic gas density, the interatomic collisions are negligible. For an atomic gas that is confined within a capillary, we can characterize the molecular flow behavior via a quantity known as the Knudsen number, Kn as

$$K_n = \frac{\lambda_{mf}}{L} \tag{A.1}$$

that is, the ratio between the mean free path $\lambda_{mf}$ of an atom that is travelling through the capillary of length $L$. The mean free path is the average distance an atom propagates before it collides. It can be quantified by

$$\lambda_{mf} \cong \frac{1}{n_0}\frac{1}{\sigma} \tag{A.2}$$

where $n_0$ is the atomic density (in units of atoms/cm$^3$) and $\sigma \cong 10^{14}$ cm$^2$ is collision cross-section, obtained by comparing the absorbed intensity with Beer's law. We can determine the atomic density from the pressure of the gas within the chamber using the ideal gas law

$$n_0 = \frac{P}{k_B T} \tag{A.3}$$

where the chamber volume is assumed to be 1 $m^3$ and for typical pressure of 760 Torr $\cong 1000mbar = 1atm = 1bar$.

At room temperature,

$$k_B T \cong 4 \cdot 10^{21} J \tag{A.4}$$

Thus, the mean free path is then at various pressure regimes, for comparison, is:

– $\lambda_{mf}(1\text{Torr}) \cong 30\mu\text{m}$

– $\lambda_{mf}(10^6\text{Torr}) \cong 30\text{m}$
$\lambda_{mf}(10^9\text{Torr}) \cong 30\text{km}$
with the typical pressure in UHV. We note that the for a dilute gas, the atoms travel distances on the order of a few kilometers while the chamber size is within a metre, such that the Knudsen number is very small.

## A.1 Flow rate

The flow of a gas within a vacuum chamber can be understood with analogues from the familiar flow of electric charge within a circuit. The flow rate $\dot{N}$ of a gas (atoms/sec) within a chain of tubes is similar to the current I within an electrical circuit. Evidently, without the influence of any other forces the atomic gas would flow from a region of high pressure $P_{high}$ to a region of low pressure $P_{low}$. While it is constrained by some resistance $R_{flow}$ due to the geometry of the vacuum system. By analogue of Ohm's law, the flow rate is

$$\dot{N} = \frac{1}{R_{flow}} (P_{high} - P_{low}) \tag{A.5}$$

where is the flow resistance $R_{flow}$ is inversely proportional to the conductivity $C$ of the system chambers.

### A.1.1 Atomic Beam & Flux

To capture as many atoms as possible with the 3D MOT beams the emergent solid angle of the atomic beam from the collection chamber must be large. This is constrained by the size of the differential pumping hole.

In the effusive flow regime, we can determine the flux of atoms emerging from a box with aperture $A$ at an angle $\theta$. The velocity distribution of a thermal cloud at equilibrium given in 3.2 for atomic velocity $v = |\vec{v}|$. However, since the probability of atoms emerging through the hole depends on the velocity of atoms, as illustrated by A.8, the velocity distribution deviates from a Maxwell-Bolzmann distribution (3.2) such that $f_v^{'}(T) \propto v^3$

$$f_v^{'}(T) = C \left(\frac{m}{k_B T}\right)^2 v^3 e^{-\frac{mv^2}{2k_B T}} \tag{A.6}$$

where $C$ is the normalization constant and the most probable velocity becomes $v_{mp} = \sqrt{3k_B T/m}$ while the mean velocity is now $\bar{v} = v_{mp}\sqrt{3\pi/8}$.For a time-interval $dt$, the volume of gas leaving the chamber is given by [41]

$$V = \bar{v} dt A \cos\theta \tag{A.7}$$

where $\bar{v} = \sqrt{8k_B T/\pi m}$ is the mean velocity, $\theta$ is the emergence angle and $A = d_1^2\pi/4$ is the aperture area with circular aperture of diameter $d_1$. The number of atoms $dN$ leavings at a solid angle $d\omega$ per unit time $dt$ is given by the flux $d\Phi$

$$dN = d\Phi dt = n\bar{v} dt A \cos\theta \frac{d\omega}{4\pi} \tag{A.8}$$

where $n$ is the number density and only a fraction $d\omega/(4\pi)$ lands on the solid angle $d\omega$. The total flux $\Phi$ out of the box is obtained by integrating over the all solid angles $d\omega = 2\pi \sin\theta d\theta$ with $\theta \in [0, \pi/2]$

$$\Phi = n\bar{v}\frac{A}{4} \tag{A.9}$$

The angular distribution leaving the cell is proportional to $\cos\theta$. Since, the majority of the atoms hit the walls of the aperture, only atoms traversing at a small angle are useful for the experiment. This approximation is valid provided that the mean free path $\lambda_{mf}$ is larger than geometry of the cell, that is in the effusive flow regime.

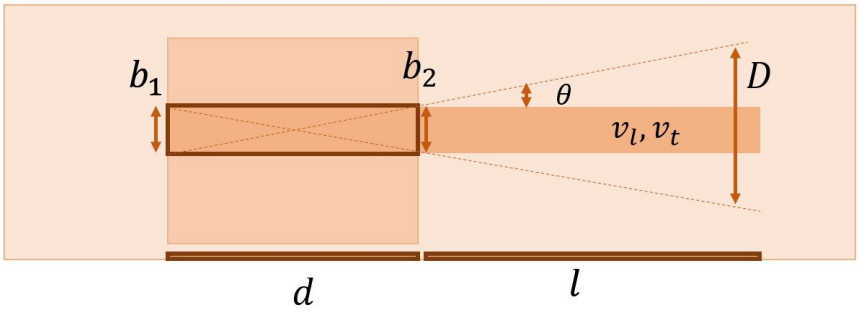


Figure A.1: Atomic beam of diameter $D$ after traversing through a hole of incident diameter $b_1$ and the exit diameter $b_2$ of length $d$. After exiting the aperture for length $l$ the atomic cloud has both transverse $v_t$ and longitudinal velocities $v_l$ that satisfy equation A.13.

Since the aperture has some finite width $d$, we can determine the angular distribution. The incident aperture has diameter $d_1$ while the decent aperture has diameter $d_2$, as shown in Fig.A.1. The beam emerges at solid angle

$$\omega = 2\pi(1 - \cos\theta) \tag{A.10}$$

where $\theta = \tan^{-1} f$ and $f = \frac{b_1/2+b_2/2}{d}$ is the collision ratio. If the MOT laser beams are at a distance $l$ from the aperture, then the diameter of the beam $D$, at distance $l$ is

$$D = 2f(d + l) - b_1 \tag{A.11}$$

and integrating over $d\omega$ with $\theta \in [0, \tan^{-1} f]$ in A.8 gives the flux through the aperture

$$\Phi' = n\bar{v}\frac{A}{4}\frac{f^2}{1+f^2} \tag{A.12}$$

Thus, there are the contributions to the velocity distribution come from the longitudinal $v_l(T)$ and the transverse velocities $v_t(T, f)$ which obey

$$v_t \leq f v_l \tag{A.13}$$

where $f$ is the collimation ratio given in A.10. The longitudinal velocity is dictated by the temperature of the ensemble whereas the transverse velocity is determined by the boundary conditions set by the aperture size and the collimation ratio $f$.

The solid angle of the atomic beam formed in our current experiment with a hole 1.5 mm in diameter and 2 mm in length is 3 radians.

# Appendix B

# Design Considerations

Some important design considerations are those of the magnetic field coils to be used to reach the Feshbach resonances and the high-NA objective. Here, we discuss the status of the design considerations for the coils.

## B.1 B-field coils

We report here the progress towards the coil design, for completeness. The coil design is proposed by Nick Mantella and Harshil Neeraj. We review here the constraints and considerations that arise when designing the coils. The magnetic field coils are designed to be able to achieve a magnetic field corresponding to the wide magnetic Feshbach resonance in $^{39}$K at 561 G with a width $\Delta = 56$ G. Simulations of bulk-machined electromagnets using the Radia package generate a field 576 G at 130 A with a pair inductance of 335 $\mu$H for 6×6 turns with an outer radius of 67.8 mm.

The magnetic field is required to be flat within the spatial range of the science chamber. Geometric constraint on the coil design is limited by the size of the laser beam and the size of the chamber. The dimensions of the science chamber are undetermined as the moment.

The generated magnetic field is time and temperature dependent. Hence, the inductance $L$ of the coil, which characterizes its dynamical response another parameter of importance.

Additionally, the Feshbach coils need a current stabilization circuit. For our current set of coils the current control is implemented through a simple IGBT switching circuit, based on Alan Stummer's design. However, since the circuit was not stored in a box, some of the connections came off, but the circuit is not functional even after re-soldering them. Thus, the stabilization circuit is currently being re-designed.

For a fixed geometry the performance is bound by the power dissipation, based room temperature copper resistivity and the wire cross-section. Based on the length of quadroupole coils in the $^{87}$Rb BEC experiment, the total resistance was estimated to be 77 m$\Omega$. This would require a 10 V power supply for a current of 130 A. The anticipated power dissipation is $I^2R = 1.301$ kW.

Large temperature fluctuations can lead to unreliable magnetic field. The hydrodynamic conductivity is determined by length and the number of windings. Larger spirals and more turns limit the limit the cooling. Ideally, the coils should not heat up by more than 5 $^{o}$C. The ability of switching between Helmholtz and anti-Helmholtz configuration is also considered. This would allow for their usage for the MOT, magnetic transfer and filtering stages as well. The required bandwidth for switching times is on the order of $\mathcal{O}$(ms). For the simulated coil configuration, the maximum current rate of change obtained is 14.9 A/ms.

### B.1.1 EDM Coil Implementation Review

The standard approach involves a hollow tube that is wound into a coil. However, this configuration is susceptible to inefficient cooling. We are pursuing bulk-machined electrogmanets for the feshbach fields in $^{39}$K.

#### B.1.1.1 Jendrzejewski Group - University of Heidelberg

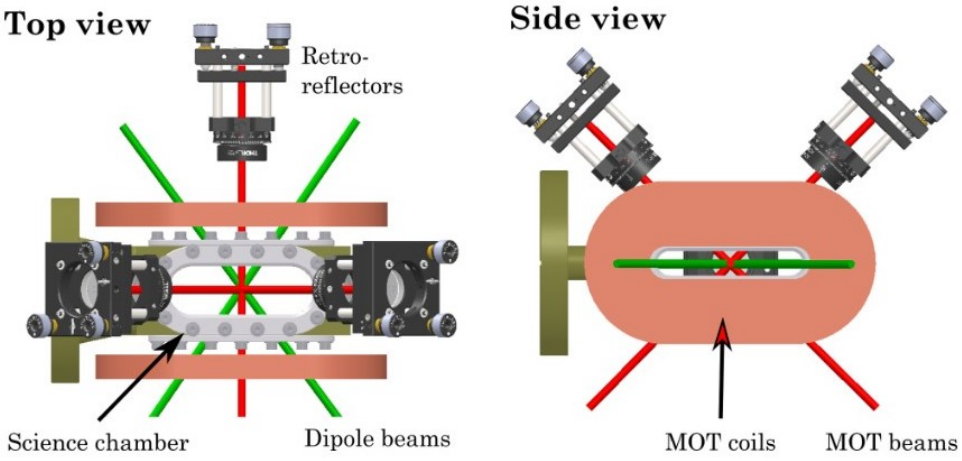


Figure B.1: CAD of the science chamber with the megnetic field coils and beams. Taken from [26].

The group in Heildelberg optimized for the following parameters in relation to the bulk-machined electromagnets for their design considerations: distance between the coils, cross-section of the coils and number of turns [26].

The magnetic field coils are driven in an anti-Helmholtz configuration. They are separated by the width $d$ of the science chamber, by 75 mm approximately. A homogeneous field gradient is observed up to a distance of $\imath = \sqrt{3}r_{eff}$ where $r_{eff}$ is effective radius of coil. Thus, the separation distance between the coils must be on the order of the effective radius of the coil, $d \leq \imath$.

The coils form an elliptical, rather than a circular cross-section that mimics the elongated shape of the viewports. To allow for large optical access the diameter of the inner radius is larger than the waist of the dipole trap beams.

The magnetic field gradient is determined by the number of turns in the coils $N$. Based on their previous set of regular coils, they adopted for 40 turns. This corresponds to 1G/cm/A of field gradient. To compactify their design, they decided on a coil pitch of 1mm/winding: a 0.3 mm layer of epoxy inserted in between a thickness of 0.7 mm copper winding. The group has since reverted to hollow coil design due to significant leakage issues.

#### B.1.1.2 Brantut Group - ETH Zurich

The Brantut group designed the bulk-machined electromagnets. Their purpose was to achieve the broad Feshbach resonance at 832.2 G in $^6$Li with width of 262 G.

They utilized the Radia package in python, to simulate their coils. They expected an inductance obtained from the simulations of 96 $\mu H$ while the measured inductance once the coils were built was 116 $\mu$H. Additionally, the expected intrinsic impedance of the coil was 8.7 m$\Omega$ and it was determined to be 10.4 m$\Omega$, measured as a function of frequency in the range of 0.16 Hz to 320 Hz [42].

They obtained a central field of 832.2 G at 325 A. The coils are separated by 104.4 mm with inner and outer radii of 32 mm and 72 mm, respectively. At the position of the atoms, their simulations predicted a field distribution of coils to vary quadratically with a curvature along the axial direction of 0.11 G/A/cm$^2$.

# Appendix C

# Control Sequence: Timing and Synchronization

For time of flight (TOF) thermometry measurements, we are using the following analog Adwin channels, some of which will be moved to digital channels later. The original TOF is written by Kelly Smith [45] and adapted by Harshil Neeraj. The image processing code is taken from the lattice experiment.

| Adwin Channel | Driver | Voltage Range |
|---|---|---|
| Ch 2 | 2D MOT repump DP AOM<br>IntraAction | Range: -0.6 to 0.6 V<br>Ideal Detuning: 102.4 MHz at 0.013V |
| Ch 3 | 2D MOT trap DP AOM<br>Isomet | Range: -1 to 1 V<br>Ideal Detuning: 122.6 MHz at -0.1 V |
| Ch 4 | Thorlabs Camera | Range: either 0V or 1V<br>(HIGH/LOW tigger can be set in<br>the Thorcam software,<br>by default on HIGH) |
| Ch 5 | 3D MOT DP trap AOM<br>Moglabs TTL | TTL: 0V = OFF; 4V = ON |
| Ch 6 | 3D MOT DP repump AOM<br>Moglabs TTL | TTL: 0V = OFF; 4V = ON |
| Ch 10 | Coils | Coil ON: 0V; Coils OFF: 3.3 V |
| Ch 11 | 3D MOT repump frequency control | Range: 0 to 7 V for 203-215 MHz<br>with precursor 209 MHz on the manual knob |
| Ch 12 | 3D MOT trap frequency control | Range: 0 to 5 V for 200-215 MHz<br>Ideal Detuning: -210 MHz at 3V<br>On resonance: 0.5 V |

# Appendix D

# Miscellaneous

When we turned on the dispenser (with pin connections A→ C) for the first time and left it on overnight some deposits formed in the interior of the 2D collection chamber, as shown in Fig.D.1. The transmission reduced upto 45 % in horizontal direction. Using UV light generated by light induced atom disorption (LIADs), tramission of 75 % was recovered. However, a similar incident did not occur when using the second dispenser (with pin connections D→ F) when left overnight. Recently, we were able to obtain a 3D MOT without having turned any of the dispensers for over three days.

## D.1 Dispensers

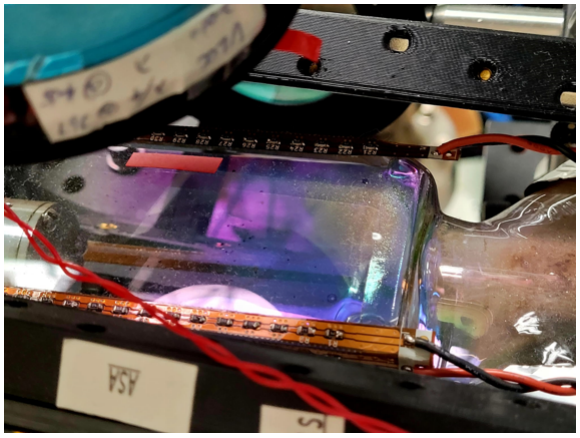

Figure D.1: Reduced transmission efficiency in the 2D collection chamber after turning SAES dispenser for 7 hours approximately.

## D.2 2D & 3D MOT Optics

The current optical set-up of the frequency shifting for the 3D MOT employs a double-pass (DP) AOM, followed by a single-pass (SP) for both the trap and the repump beams, providing a total shift of 240 MHz and 203 MHz, respectively. For the 2D MOT frequency shifting two DP AOMs are employed, one for trap and another for repumper. The following re-design, in Fig. D.2, avoids the use of DP and SP configuration in 3D optics, and generates a combined beam for the 2D and the 3D MOTs light which reduces the number of AOMs used from four to only two for the entire $D_2$ optics. Also, the push beam in the current set-up is some light re-directed from the 2D MOT optics and it does not have independent frequency and power control whereas the new design allows for control of the push beam. However, a limitations of the set-up shown below is that inability to independently control the 2D MOT and 3D MOT trap and re-pumper beams remotely.

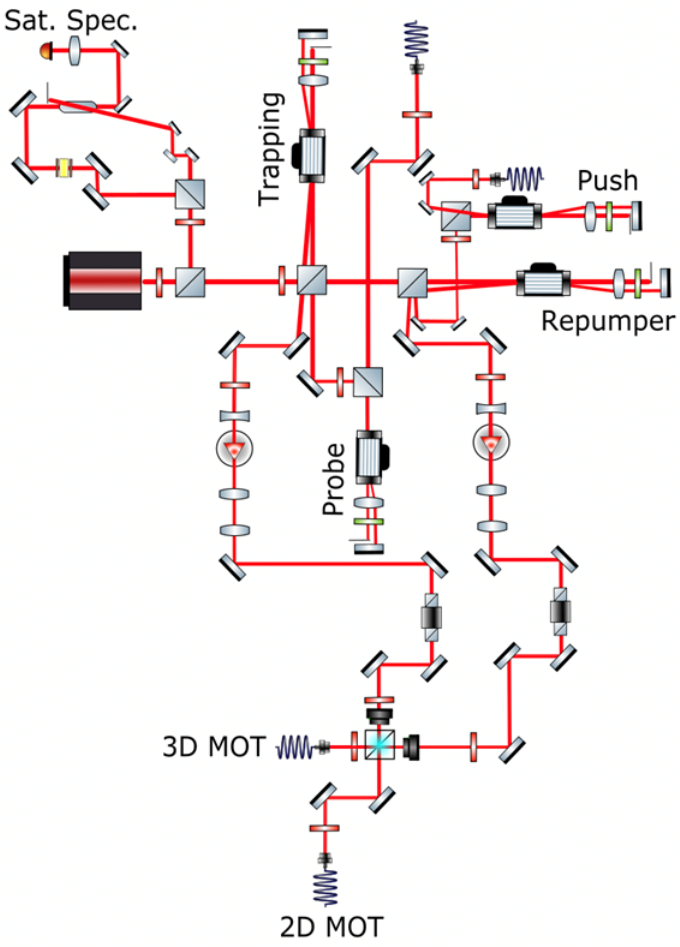


Figure D.2: Re-design of $D_2$ optics. Courtesy of N. Mantella.

# Bibliography


[1] P. Adlarson, W. Augustyniak, W. Bardan, M. Bashkanov, F. Bergmann, M. Berłowski, H. Bhatt, M. Büscher, H. Calen, I. Ciepał et al. , *Physical review letters* **112** (2014), 202301.

[2] A. Aspect, E. Arimondo, R.e.a. Kaiser, N. Vansteenkiste und C. Cohen-Tannoudji, *Physical Review Letters* **61** (1988), 826.

[3] M. Bashkanov und D. Watts, *Journal of Physics G: Nuclear and Particle Physics* **47** (2020), 03LT01.

[4] M. Büttiker und R. Landauer, *Physica Scripta* **32** (1985), 429.

[5] R. Carles und G. Ferriere, *arXiv preprint arXiv:2209.14621* (2022).

[6] C. Chin, R. Grimm, P. Julienne und E. Tiesinga, *Reviews of Modern Physics* **82** (2010), 1225.

[7] S. Chu, L. Hollberg, J.E. Bjorkholm, A. Cable und A. Ashkin, *Physical review letters* **55** (1985), 48.

[8] C. Cohen-Tannoudji, *Fundamental systems in quantum optics* **53** (1990), 1.

[9] C. Cohen-Tannoudji und D. Guéry-Odelin, (2011).

[10] C.N. Cohen-Tannoudji, *Reviews of Modern Physics* **70** (1998), 707.

[11] J. De Laeter, K. Heumann und K. Rosman, *Journal of physical and chemical reference data* **20** (1991), 1327.

[12] S.O. Demokritov, V.E. Demidov, O. Dzyapko, G.A. Melkov, A.A. Serga, B. Hillebrands und A.N. Slavin, *Nature* **443** (2006), 430.

[13] C. d'Errico, M. Zaccanti, M. Fattori, G. Roati, M. Inguscio, G. Modugno und A. Simoni, *New Journal of physics* **9** (2007), 223.

[14] B. Divinskiy, H. Merbouche, V. Demidov, K. Nikolaev, L. Soumah, D. Gouéré, R. Lebrun, V. Cros, J.B. Youssef, P. Bortolotti et al. , *Nature communications* **12** (2021), 6541.

[15] L. Dupays, D.C. Spierings, A.M. Steinberg und A. del Campo, *Physical Review Research* **3** (2021), 033261.

[16] J. Dupont-Roc, G. Grynberg et al. , *Basic Processes and Appli* (1992).

[17] J. Etrych, G. Martirosyan, A. Cao, J.A. Glidden, L.H. Dogra, J.M. Hutson, Z. Hadzibabic und C. Eigen, *Physical Review Research* **5** (2023), 013174.

[18] S. Falke, H. Knöckel, J. Friebe, M. Riedmann, E. Tiemann und C. Lisdat, *Physical Review A* **78** (2008), 012503.

[19] C.J. Foot: *Atomic physics*, Band 7. OUP Oxford, 2004.

[20] L. Fouché: *Gaz quantiques de potassium 39 à interactions contrôlables*. Palaiseau, Institut d'optique théorique et appliquée, Dissertation, 2015.

[21] R. Grimm, M. Weidemüller und Y.B. Ovchinnikov. In *Advances in atomic, molecular, and optical physics*, Band 42. Elsevier (2000), Seiten 95–170.

[22] T.W. Hänsch und A.L. Schawlow, *Optics Communications* **13** (1975), 68.

[23] P.C. Hohenberg, *Physical Review* **158** (1967), 383.

[24] B.C. Hsu. *About Our Third Vacuum System* (2018). Thywissen Lab Summer Report.

[25] F. Huang, Z.Y. Zhang, P.N. Shen und W.L. Wang, *Chinese Physics C* **39** (2015), 071001.

[26] R.P.B. Jan Kilinc, Lilo Höcker. *Making water-cooled magnetic field coils* (2021). SynQS.

[27] L.A.N. Laboratory. *Potassium* (2021). U.S. Department of Energy.

[28] H. Lin. *Design and Optimization of a 39K 2D-MOT Atom Source* (2020). University of Toronto, Undergrad- uate Thesis.

[29] N. Mantella, J. McGowan IV, H. Neeraj, D. Spierings und A. Steinberg: *An Atomic Fabry-Perot for the Generation and Measurement of Ultracold Wavepackets. An Atomic Fabry-Perot for the Generation and Measurement of Ultracold Wavepackets*, In *APS Division of Atomic, Molecular and Optical Physics Meeting Abstracts*, Band 2022. (2022) Seiten F01–088.

[30] A. Marte, T. Volz, J. Schuster, S. Dürr, G. Rempe, E. Van Kempen und B. Verhaar, *Physical Review Letters* **89** (2002), 283202.

[31] B. Mercier, *Journal of Vacuum Science & Technology A: Vacuum, Surfaces, and Films* **24** (2006), 529.

[32] H.J. Metcalf und P. Van der Straten: *Laser cooling and trapping*. Springer Science & Business Media, 1999.

[33] T. Nikuni, M. Oshikawa, A. Oosawa und H. Tanaka, *arXiv preprint cond-mat/9908118* (1999).

[34] J.F. O'Hanlon: *A user's guide to vacuum technology*. John Wiley & Sons, 2005.

[35] C.J. Pethick und H. Smith: *Bose–Einstein condensation in dilute gases*. Cambridge university press, 2008.

[36] W. Phillips, *J. Dalibard, JM Raimond,,, and J. Zinn-Justin, editors, Fundamental Systems in Quantum Optics* (1992), 165.

[37] C. Pür, M. Hetzel, M. Quensen, A. Hüper, J. Geng, J. Kruse, W. Ertmer und C. Klempt, *Physical Review A* **107** (2023), 033303.

[38] H. Ramachandran und K.G. Li. *Laser-cooling* $^{39}K Atoms with D2$ *and* $D_1$ *Light* (2001). Thywissen Lab Summer Report.

[39] R. Ramos, D. Spierings, S. Potnis und A.M. Steinberg, *Physical Review A* **98** (2018), 023611.

[40] R. Ramos, D. Spierings, I. Racicot und A.M. Steinberg, *Nature* **583** (2020), 529.

[41] N.F. Ramsey, *New York* (1985).

[42] K. Roux, B. Cilenti, V. Helson, H. Konishi und J.P. Brantut, *SciPost Physics* **6** (2019), 048.

[43] G. Salomon, L. Fouché, P. Wang, A. Aspect, P. Bouyer und T. Bourdel, *Europhysics Letters* **104** (2014), 63002.

[44] T.C. Scott und K.G. Zloshchastiev, *Low Temperature Physics* **45** (2019), 1231.

[45] E. Sequencing. *E3 Sequencing* (2021). Thywissen Lab Summer Report.

[46] B. Shammout: *A Laser System for Gray-Molasses Cooling on the D1 Transition of an Atomic Gas of 39K*. Hannover: Gottfried Wilhelm Leibniz Universität, Diplomarbeit, 2020.

[47] D.A. Steck, (2007).

[48] A.M. Steinberg, *Physical Review A* **52** (1995), 32.

[49] A.M. Steinberg, *Physical review letters* **74** (1995), 2405.

[50] F. Stubenrauch. *Frequency Modulation Saturation Spectroscopy Laser Lock of An Interference-Filter-Stabilized External-Cavity Diode Laser* (2010). Research Report.

[51] J.R. Taylor: *Scattering theory: the quantum theory of nonrelativistic collisions.* Courier Corporation, 2006.

[52] R. Thomas und N. Kjærgaard, *Review of Scientific Instruments* **91** (2020).

[53] T. Tiecke, *University of Amsterdam, The Netherlands, Thesis* (2010), 12.

[54] D.C. Spierings van der Wolk: *Precise Larmor Time Measurements of a Tunneling Bose-Einstein Condensate.* Dissertation, 2022.

[55] X. Xia: *Towards a more reliable ultracold mixture platform.* Dissertation, 2022.

[56] X.C. Yao, R. Qi, X.P. Liu, X.Q. Wang, Y.X. Wang, Y.P. Wu, H.Z. Chen, P. Zhang, H. Zhai, Y.A. Chen et al. , *Nature Physics* **15** (2019), 570.

# Acknowledgements

Prof. Joseph Thywissen. I am honoured to have had the opportunity to learn from you. Your enthusiasm is inspiring! Thank you for our fireside discussions.

Prof. Aephraim Steinberg, thank you for the opportunity of letting me join the Steinberg Journal Club meetings.

Foremost, thank you to Nick and Harshil for teaching me most of the things I know. It has been a great team! Thank you Mohid and Moji, you have been a great addition to the team over the summer. For the times when the senior E3 members were not around, I received an immense support from all the Thywissen lab members. So, thank you!!! To all the Chip experiment guys: Kenneth, Colin, Kevin and Kiera; and the Lattice experimentalists to Frank, Robyn, Ben and legendary Cora.

From the Steinberg lab, I would like to thank Joseph M., Daniela A., Batuhan Y., Vida N. and Andy J. - our occasional discussions have been very insightful.

Thank you to family, friends and loved ones for all their support!!!